

# Sn-Triggered Two-Dimensional Fast Protein Assembly with Emergent Functions

Bassam Saif,<sup>†</sup> Wenxin Zhang,<sup>‡</sup> Xu Zhang,<sup>‡</sup> Quan Gu,<sup>\*,†</sup> and Peng Yang<sup>\*,†</sup>

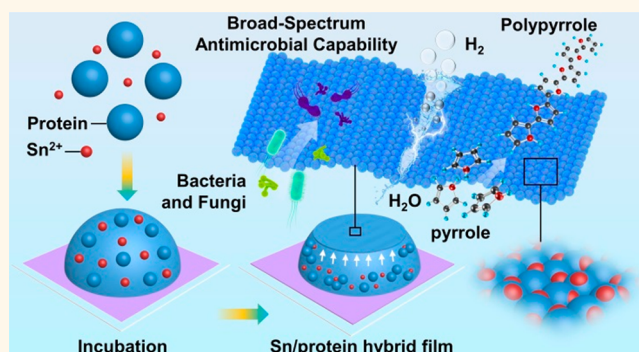
<sup>†</sup>Key Laboratory of Applied Surface and Colloid Chemistry, Ministry of Education, School of Chemistry and Chemical Engineering, Shaanxi Normal University, Xi'an 710062, P.R. China

<sup>‡</sup>School and Hospital of Stomatology, Tianjin Medical University, 12 Observatory Road, Tianjin 30070, P.R. China

## Supporting Information

**ABSTRACT:** The discovery of a general strategy for organizing functional proteins into stable nanostructures with the desired dimension, shape, and function is an important focus in developing protein-based self-assembled materials, but the scalable synthesis of such materials and transfer to other substrates remain great challenges. We herein tackle this issue by creating a two-dimensional metal–protein hybrid nanofilm that is flexible and cost-effective with reliable self-recovery, stability, and multifunctionality. As it differs from traditional metal ions, we discover the capability of  $\text{Sn}^{2+}$  to initiate fast amyloid-like protein assembly (occurring in seconds) by effectively reducing the disulfide bonds of native globular proteins. The  $\text{Sn}^{2+}$ -initiated lysozyme aggregation at the air/water interface leads to droplet flattening, a result never before reported in a protein system, which finally affords a multifunctional 2D Sn-doped hybrid lysozyme nanofilm with an ultralarge area (e.g.,  $0.2 \text{ m}^2$ ) within a few minutes. The hybrid film is distinctive in its ease of coating on versatile material surfaces with enduring chemical and mechanical stability, optical transparency, and diverse end uses in antimicrobial and photo-/electrocatalytic scaffolds. Our approach provides not only insights into the effect of tin ions on macroscopic self-assembly of proteins but also a controllable and scalable synthesis of a potential biomimic framework for biomedical and biocatalytic applications.

**KEYWORDS:** metalloproteins, tin, amyloid-like assembly, hybrid nanofilm, biocatalytic scaffold



The self-assembly of peptides and proteins has recently emerged as a method to create structurally defined, physically robust two-dimensional (2D) nanoscale assemblies, which have significant implications for both biology and technology.<sup>1,2</sup> In contrast to peptide-based systems, proteins possess considerably more structural and chemical complexity, and therefore, the programming of a protein assembly into a supramolecular architecture is often not straightforward and much more challenging than the process for peptides.<sup>3,4</sup> In particular, assembling a homogeneous macroscopic proteinaceous 2D material at a meter scale or more to truly rival a natural object generally of giant size remains a challenge.<sup>5</sup> Moreover, low assembly efficiency and speed impede scalable production for practical industry use.<sup>5</sup> Herein, we reveal a strategy using metal-directed protein assembly to tackle the above issues and to obtain a robust 2D metal-doped hybrid protein nanofilm with an ultralarge area (e.g.,  $0.2 \text{ m}^2$ ), a simple and superfast preparation process (occurring in seconds), diverse functions, and enduring stability.

Metal ions are of prime importance to over one-third of all native proteins in nature through associations, and such intrinsic metal atoms provide catalytic, regulatory, or structural roles critical to protein functions.<sup>6</sup> These metalloproteins (MPs) thus play a vital role in many crucial cellular processes ranging from photosynthesis and drug metabolism to respiration and water oxidation. In this context, tremendous efforts have been made toward the design of MPs mimics and related materials for countless technological applications such as catalysis, biosensors, biomemory, and bioelectronics.<sup>7–15</sup> However, most of the strategies are relatively complex, of low efficiency, and not suitable for large-scale engineered applications.<sup>16–21</sup> In particular, although precise designs for the self-assembly of MPs, such as 1D nanotubes or 2D crystalline arrays, have recently emerged,<sup>22,23</sup> the scalable synthesis of MP-derived materials, e.g., 2D free-standing

Received: February 19, 2019

Accepted: June 18, 2019

Published: June 18, 2019

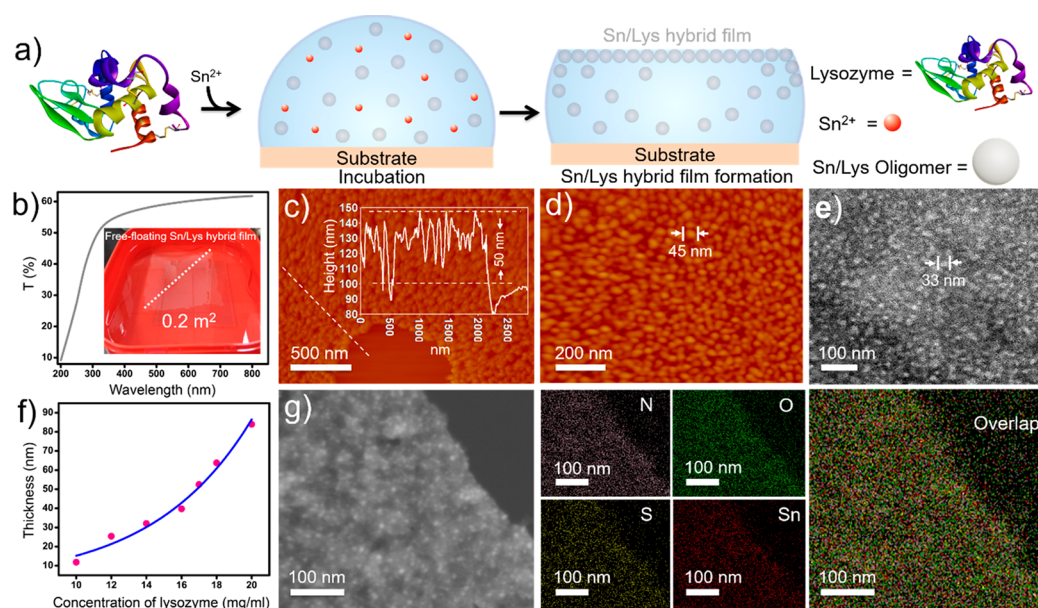


**Figure 1.** Formation and characterization of the Sn/Lys hybrid film. (a) Schematic representation of tin-directed protein self-assembly into the Sn/Lys hybrid film. (b) UV/vis spectrum of the Sn/Lys hybrid film with the inset showing a large-area hybrid film at the air/water interface. (c, d) Typical thickness (c) and surface morphology (d) of the Sn/Lys hybrid film characterized by AFM. (e) TEM image of the Sn/Lys hybrid film. (f) Plot of the thickness of the Sn/Lys hybrid film as a function of lysozyme concentration (SnCl<sub>2</sub>, 0.1 M). (g) STEM image and corresponding EDS elemental mapping of N, O, S, and Sn of the Sn/Lys hybrid film, respectively.

nanofilm, and their robust transfer to various substrates have not been documented due to the difficulty of the controllable and fast amplification of metal-biomolecular assemblies. Actually, the favorable interplay between metal and protein as widely exists in nature is not easily copied in synthetic systems, in which protein denaturation to uncontrolled precipitates is often induced by metal ions (especially notorious for heavy metal ions). Such limitations usually lead to the great challenge and low efficiency of designing and synthesizing metal/protein hybrid materials. Unlike simple protein denaturation, we herein report the finding that heavy metal ions (even in high concentration) may drive controllable protein assembly at the air/water interface to result in functional hybrid materials. As a result, we underline the capability of Sn<sup>2+</sup> to initiate fast amyloid-like protein assembly (occurring in seconds) by effectively reducing the disulfide bonds of native globular proteins.

Unlike the wide use of some metal ions such as Co<sup>2+</sup>, Ni<sup>2+</sup>, Cu<sup>2+</sup>, Zn<sup>2+</sup>, Fe<sup>2+</sup>, Mg<sup>2+</sup>, and Ca<sup>2+</sup> in conventional MP-mimicking systems,<sup>24</sup> our present strategy is based on the use of tin ions (Sn<sup>2+</sup>) and their capability to initiate fast and controllable protein assembly. It is surprising that Sn, as a natural metal element, has been much less explored in the field of MPs and relative assembly. Indeed, it is widely believed that Sn and its derivatives, such as highly active semiconductor SnS<sub>2</sub>, have long been exploited in daily human life in food manufacturing, toothpaste, radiopharmaceuticals, and therapeutic agents as well as being key in a wide range of technological applications, including gas-sensing, semiconductor, and energy storage systems.<sup>25–29</sup> For protein assembly, the question arises of how to effectively integrate Sn with proteins to produce well-defined scalable nanostructures that are flexible and cost-effective with multifunctionality and good stability. On the basis of our recent understanding of amyloid-like protein assembly,<sup>5,30–33</sup> herein we reveal that the selective reduction of disulfide bonds in hen egg white lysozyme

(HEWL) could be efficiently performed by Sn<sup>2+</sup> ions to result in rapid amyloid-like assembly into Sn/protein 2D hybrid nanofilms flattening at the air/water interface (Figure 1a). Previous reports from our and other groups indicated that metal ions such as Ag<sup>+</sup>, Cu<sup>2+</sup>, Fe<sup>2+</sup>, and Zn<sup>2+</sup> could promote the formation of amyloids by triggering the nucleation and stabilize the amyloids by preventing further growth.<sup>30,34–36</sup> In the present work, the binding of Sn<sup>2+</sup> with lysozyme facilitates the unfolding and aggregation (nucleation) of lysozyme to form oligomers. Such oligomers hybridized (stabilized) by Sn<sup>2+</sup> are further aggregated at the air/water interface to form the 2D film (Figure 1a). This kind of biomimicking MP material can be easily transferred onto a wide variety of substrates such as silicon, glass, metals, and organic polymers, with robust interfacial adhesion and chemical stability. HEWL is a 129-residue globular protein containing four disulfide bridges to stabilize the molecule and mainly consists of two-domain structures including  $\alpha$ -helices and  $\beta$ -sheets. This protein is attractive for the design of engineered MP materials because of its high stability, low cost, and wide availability, but nonetheless, a great challenge also remains in converting such a nonmetalloprotein into MP materials. The purpose of our design is to engineer the assembly and development of bioinspired hybrid materials for applications in biocatalytic systems and beyond. We finally demonstrate that besides HEWL, a series of globular nonmetalloproteins could be similarly triggered by Sn<sup>2+</sup> into rapid assembly to form 2D hybrid nanofilms.

## RESULTS AND DISCUSSION

Our design strategy is schematically illustrated in Figure 1a, in which a Sn/Lys hybrid film was formed at the air/water interface within a few minutes by mixing tin chloride (SnCl<sub>2</sub>, typically 0.1 M) in solution with HEWL buffer (typically 17 mg/mL) at room temperature. The film was colorless with certain optical transparency and could be easily prepared in a

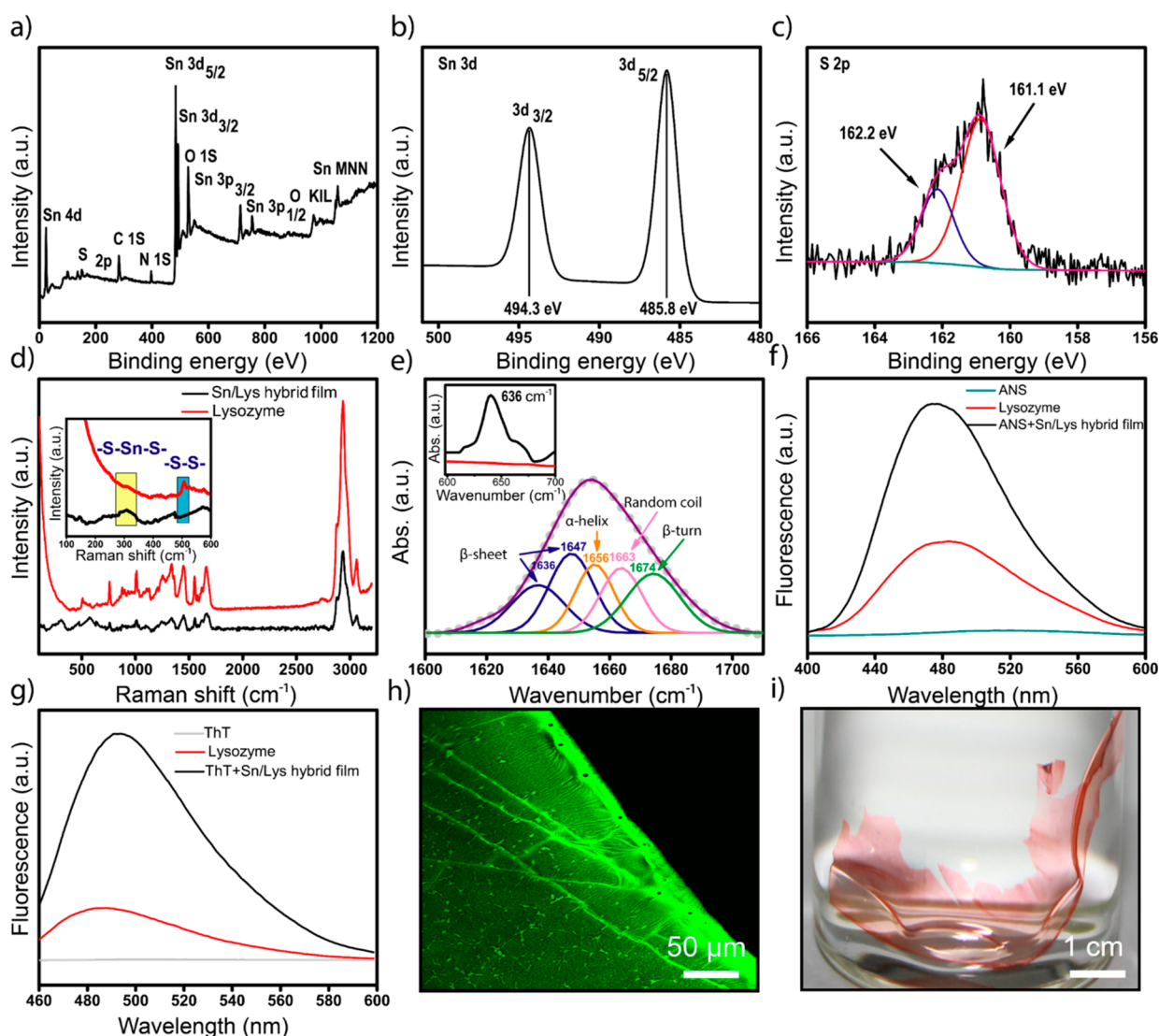


**Figure 2.** Structural characterization of the Sn/Lys hybrid film. (a–c) Survey (a) and high-resolution XPS spectra of Sn<sub>3d</sub> (b) and S<sub>2p</sub> (c) on the hybrid film. (d) Raman spectra of native lysozyme and the Sn/Lys hybrid film, with the inset showing the characteristic peaks for the clusters of –S–Sn<sub>x</sub>–S– at 309 cm<sup>-1</sup> and reduction of the disulfide bond at 505 cm<sup>-1</sup>, respectively. (e) Deconvolution of the amide I band in the FT-IR spectrum of the Sn/Lys hybrid film, with the inset showing the peak at 636 cm<sup>-1</sup> assigned to the formation of –S–Sn(II)<sub>x</sub>–S– clusters in the hybrid film. (f) The fluorescence spectra of the ANS buffer, the mixed buffer of ANS and native lysozyme, and the Sn/Lys hybrid film dyed by ANS. (g) The fluorescence spectra of the ThT buffer, the mixed buffer of ThT and native lysozyme, and the Sn/Lys hybrid film dyed by ThT. (h) The corresponding fluorescence microscopic image of the Sn/Lys hybrid film after dying by ThT. (i) The corresponding digital photograph of the Sn/Lys hybrid film after dying by Congo red.

large area (e.g., 0.2 m<sup>2</sup>) since its size was simply controlled by the air/water interface area (Figure 1b). Atomic force microscopy (AFM) and scanning electron microscopy (SEM) images revealed that the typical thickness of the hybrid film was 50 nm (Figure S1 and Figure 1c), and high-magnification AFM analysis further reflected that the hybrid film was composed of close-packed nanoparticles with an average diameter of 45 ± 3 nm (Figure 1d). Transmission electron microscopy (TEM) provided a slightly lower measurement than that from AFM, showing nanoparticles with an average diameter of 33 ± 5 nm homogeneously dispersed in the hybrid film (Figure 1e). This difference might be due to possible deformation from the tip during the tapping-mode scan of AFM. The approaching size between the film thickness and internal particle diameter implied that the film was close to a 2D assembly of nanoparticles. Moreover,

the film thickness could be finely modulated, e.g., from 10 to more than 80 nm, by increasing the lysozyme concentration from 10 to 20 mg/mL or by controlling the reaction time (Figure S2). Such results indicated that the assembly into the film could be tailored from a single layer to several layers of nanoparticles (Figure 1f). The corresponding root-mean-square (RMS) was also well controlled from 3 to 10 nm by the lysozyme concentration, indicating a relatively flat morphology of the film surface (Figure S3). The scanning transmission electron microscopy (STEM)-based elemental mapping further suggested the presence of N, O, S, and Sn components in the film, implying the dispersion of Sn-based clusters in the hybrid film (Figure 1g).<sup>37</sup>

In conventional recognition, most soluble proteins precipitate in the presence of high concentrations of transition metals because simultaneous binding of multiple metal ions on the

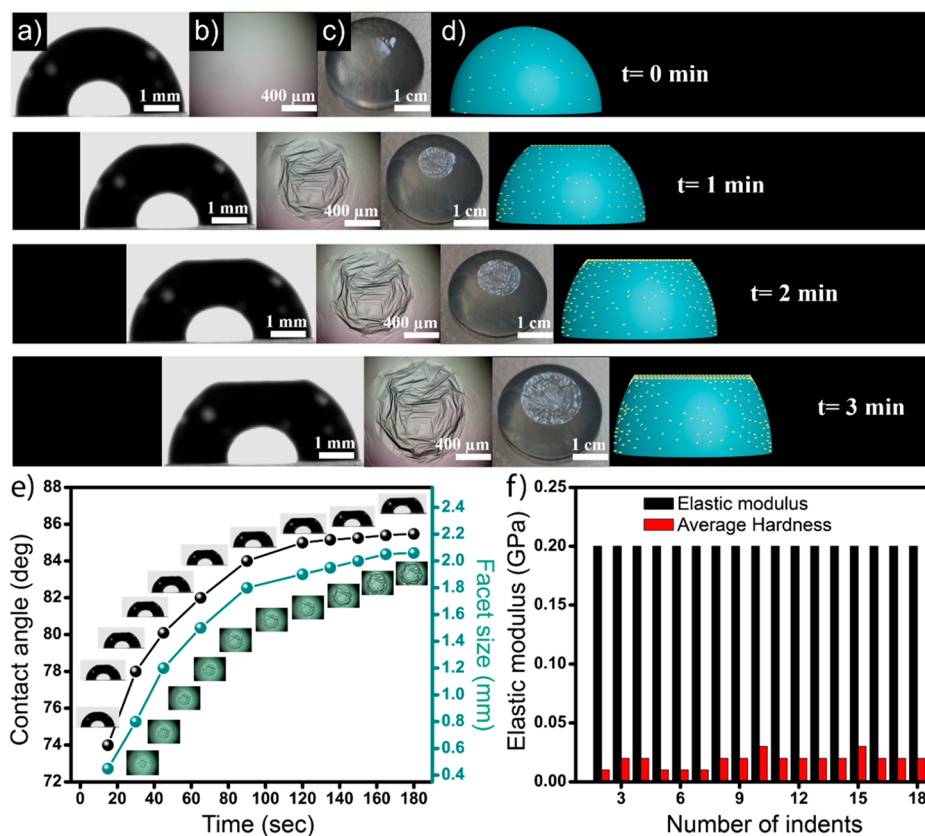


**Figure 3.** Facet formation of the Sn/Lys hybrid film on top of the reaction solution droplet. (a–d) Side view (a) and top view (b) from the optical microscope, top view from the digital camera (c), and cartoon (d) to show the faceting on top of the reaction solution droplet *via* formation of the Sn/Lys hybrid film on the droplet at the time scale of 0–3 min. (e) Changes in the faceting size and contact angle of the buffer droplet with Sn/Lys hybrid film as a function of reaction time. (f) Elastic modulus and surface hardness of the Sn/Lys hybrid film in multiple indents at a strain rate of  $0.05 \text{ s}^{-1}$ .

protein surface would result in the formation of heterogeneous mixtures of metal-cross-linked biopolymers.<sup>38</sup> The assembly into a well-defined nanofilm triggered by  $0.1 \text{ M SnCl}_2$  in the present work was contrary to conventional knowledge, suggesting a controlled interaction between  $\text{Sn}^{2+}$  and lysozyme. Actually, HEWL has redox-active cysteine (Cys) residues, which not only can maintain the native conformation of proteins through the formation of intramolecular disulfide bonds<sup>39,40</sup> but also provide a powerful means to bind with metals for specific functions (*e.g.*, biocatalytic activity).<sup>41,42</sup> We hypothesized that the high affinity of Cys residues to  $\text{Sn}^{2+}$  played a crucial role in the coordination, stabilization, and rapid formation of the thermodynamically favored hybrid film.<sup>29,43–45</sup> X-ray photoelectron spectroscopy (XPS) and Raman evidence provided support to this hypothesis (Figure 2a–d). The survey XPS spectrum showed the presence of Sn, C, N, O, and S in the hybrid film without other elements detected (Figure 2a). The high-resolution C 1s spectrum reflected the primary protein chain structure (*e.g.*, amide, ester, amine, thiol groups) in the film (Figure S4). Two strong peaks located at 485.8 and 494.3 eV were found and assigned to the  $\text{Sn}_{3d_{5/2}}$  and  $\text{Sn}_{3d_{3/2}}$  of  $\text{Sn}^{2+}$  (Figure 2b),<sup>46</sup> which suggested the existence of  $\text{Sn}^{2+}$  in the hybrid film. From Figure 2c, the deconvoluted  $\text{S}_{2p}$  was at 161.1 and 162.2 eV, which could be attributed to the interaction between S (Cys) of lysozyme and  $\text{Sn}^{2+}$ .<sup>46</sup> Based on the Raman spectra, it was found that the disulfide bond of lysozyme at  $505 \text{ cm}^{-1}$  was reduced with the addition of  $\text{Sn}^{2+}$  (Figure 2d), which was reasonably ascribed to

the reduction activity of  $\text{Sn}^{2+}$  toward the disulfide bond of Cys–Cys at low pH.<sup>47</sup> Moreover, the new band appearing at  $309 \text{ cm}^{-1}$  was assigned to the structure of  $-\text{Cys}-\text{Sn}(\text{II})_x-\text{Cys}-$ , which suggested the formation of  $-\text{C}-\text{S}-\text{Sn}(\text{II})_x-\text{S}-\text{C}-$  clusters (Figure 2d).<sup>48</sup> The Raman band for the  $-\text{Cys}-\text{Sn}(\text{II})_x-\text{Cys}-$  structure shifted five to six wavenumbers lower compared to that of bulk  $\text{SnS}_2$ , which was probably due to the valence difference ( $\text{Sn}^{2+}$  in the  $-\text{Cys}-\text{Sn}(\text{II})_x-\text{Cys}-$  vs  $\text{Sn}^{4+}$  in  $\text{SnS}_2$ ) and phonon confinement effect in the 2D Sn/Lys hybrid nanofilm compared to the bulk  $\text{SnS}_2$ .<sup>48,49</sup> Multiple functional groups exposed on the surface of the Sn/Lys hybrid film were also characterized by Raman analysis (Figure S5), which was favorable to further sequential surface chemical derivatization (*e.g.*, the protein–Sn coordination reported herein) and robust adhesion of the film to various material surfaces (as shown below).<sup>50</sup> The significant presence of specific amino acid residues on the Sn/Lys hybrid film was identified by Raman spectral deconvolution analysis (Figure S6). The propensity of phenylalanine (Phe), tryptophan (Trp) and tyrosine (Tyr) residues on the Sn/Lys hybrid film were approximately 2-fold higher for Phe and 3-fold higher for Trp and Tyr, respectively, than those from native lysozyme (Figure S6).

Overall, the above results indicated that the divalent tin ion triggered reduction of the intramolecular disulfide of lysozyme, a result never before reported. The conformational change of the protein in the hybrid film was further examined using Fourier transform infrared spectrometry (FT-IR). The FTIR bands at  $1656$  and  $1537 \text{ cm}^{-1}$  appeared in the hybrid film as an

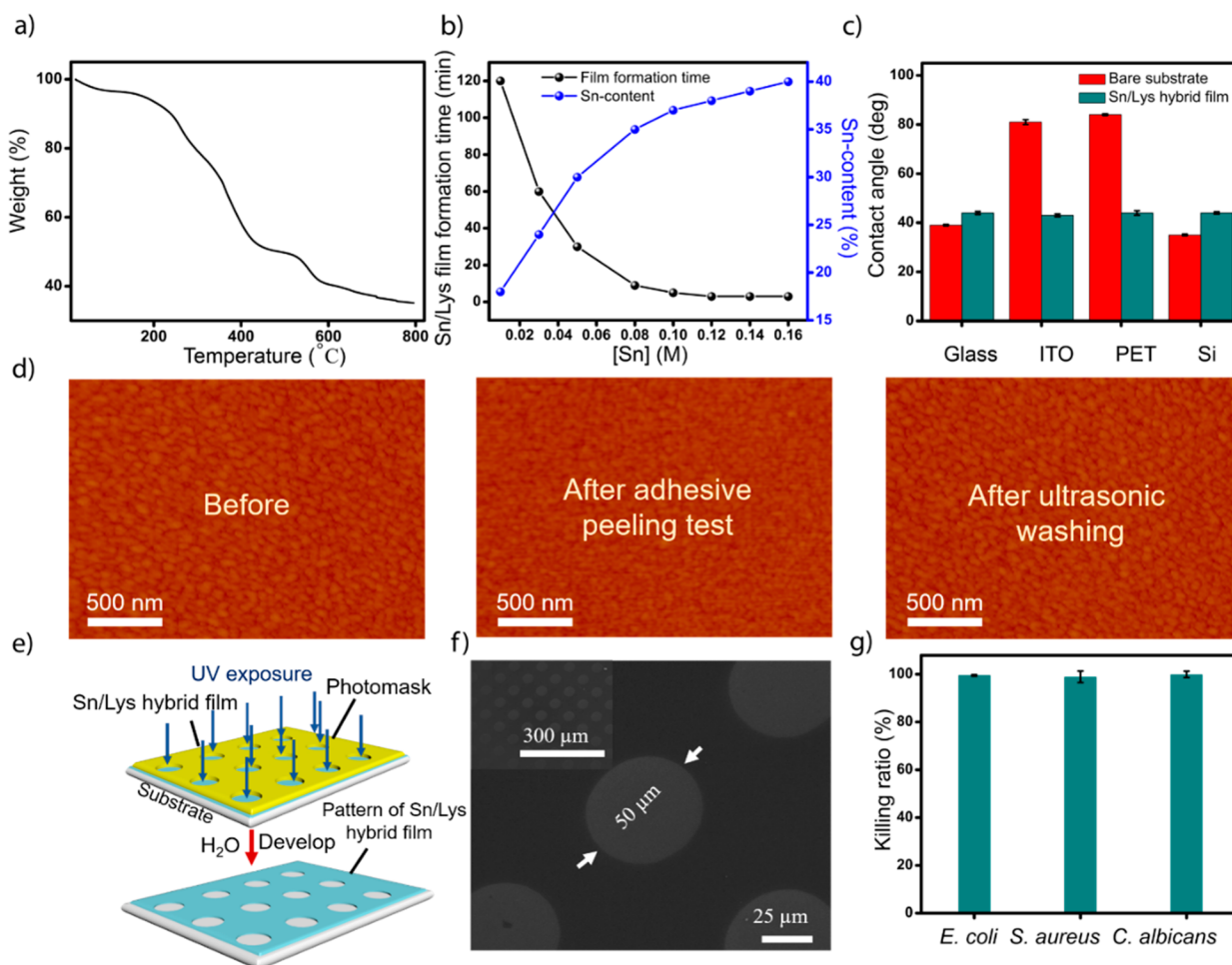


**Figure 4.** (a) Thermogravimetric (TG) analysis of the Sn/Lys hybrid film. (b) Film formation time and content of Sn in the Sn/Lys hybrid film as determined by TG analysis. (c) WCA of the Sn/Lys hybrid film coated onto various substrates. (d) Typical AFM images of the Sn/Lys hybrid film coated onto glass substrates before (left), after 3 M Scotch adhesive tape peeling (middle), and after ultrasonication washing in a water bath for 30 min (50 kHz, 200 W) (right), respectively. (e) Schematic illustration of UV exposure-induced micropatterning on the Sn/Lys hybrid film. (f) SEM image showing the Sn/Lys hybrid film with micropatterning on the silicon substrate. (g) Killing ratio of the Sn/Lys hybrid film toward *E. coli*, *S. aureus*, and *C. albicans*, respectively.

amide I stretching vibration and an amide II bending vibration, respectively (Figure S7). In contrast to native lysozyme, a new peak was observed at  $636\text{ cm}^{-1}$  in the hybrid film due to the interaction between  $\text{Sn}^{2+}$  and the Cys residues of lysozyme (Figure 2e).<sup>51</sup> The deconvoluted FT-IR spectra of the amide I band confirmed the presence of  $\beta$ -sheet stacking ( $1636$  and  $1647\text{ cm}^{-1}$ ) in the hybrid film (Figure 2e).<sup>52</sup> In the above spectra of Raman, FTIR, and XPS analysis, the signals for Sn–O bond between  $\text{Sn}^{2+}$  and O (Asp) of lysozyme (at  $113$  and  $211\text{ cm}^{-1}$  in Raman,  $560\text{ cm}^{-1}$  in FTIR)<sup>53,54</sup> and signals for the Sn–N bond between  $\text{Sn}^{2+}$  and N (His) of lysozyme (at  $397.5\text{ eV}$  in XPS)<sup>55</sup> were absent (Figure 2d, Figures S7 and S8). Such results then reflected that a possible interaction between  $\text{Sn}^{2+}$  and amino acids other than cysteine (e.g., Asp and His) was not predominant in the present model. The interaction between  $\text{Sn}^{2+}$  and cysteine was further supported by the control experiment in which proteins without disulfide (S–S) bonds (e.g., myoglobin and cytochrome c) were used to mix with tin ions. The results showed no Sn/protein hybrid films formed after the treatment by  $\text{Sn}^{2+}$ , which indicated the important role of S–S bond in the present model. Anilino-1-naphthalene sulfonate (ANS) was utilized as a fluorescent probe to monitor the exposure and aggregation of hydrophobic

residues in the protein after binding with  $\text{Sn}^{2+}$  (Figure 2f, Figure S9). The ANS fluorescence intensity increased rapidly after the addition of  $\text{Sn}^{2+}$  into the protein buffer, which reflected the hydrophobic exposure and aggregation of HEWL due to unfolding.<sup>56</sup> In such a process, at least the exposure and aggregation of hydrophobic residues such as Trp on the surfaces of oligomers contributed to the aggregation and formation of the 2D film at the air/water or liquid/solid interfaces.<sup>5</sup> The assembly process was further monitored using a ThT assay, applying a specific fluorescent dye to bind with amyloid-like antiparallel  $\beta$ -sheet stacking.<sup>57</sup> When tin ions were introduced into the protein buffer, the ThT fluorescence intensity of the solution increased significantly, with a redshift of its peak from  $484$  to  $493\text{ nm}$  (Figure 2g, Figure S10). The fluorescence enhancement on the hybrid film after ThT staining was also visually confirmed by fluorescence microscopy imaging (Figure 2h, Figure S11). The formation of  $\beta$ -sheets was further confirmed by Congo red staining (Figure 2i). The above results implied that the binding of  $\text{Sn}^{2+}$  to Cys residues reduced the disulfide bond of lysozyme and then induced the unfolding and aggregation of HEWL to form amyloid-like  $\beta$ -sheet stacking.

The incorporation of metal ions into the protein nanofilm endowed the material with relatively high mechanical strength, which consequently pressed the droplet to result in the droplet flattening (Figure 3, Figure S12). The wrinkles observed around the droplet also indicated the flexibility of the hybrid film (Figures S12–S14). This flattening behavior has only been previously reported with the use of synthetic peptides<sup>58</sup> or polydopamines.<sup>59</sup> Upon mixing of the lysozyme buffer with SnCl<sub>2</sub> solution, typically after 1 min, the hybrid nanofilm was clearly observed on the droplet surface, and the newly formed nanofilm strongly flattened the top of the buffer droplet into a flat plane (Figure 3a–d, movie S1). The faceting speed was very fast, since the initial small facet was observed at ~15 s after the two buffers were mixed, and then the faceting size (*i.e.*, the hybrid film size) was quickly enlarged within ~180 s to nearly 5 times larger than the beginning size (Figure 3e). As revealed in our previous study on the mechanism of fast amyloid-like lysozyme assembly, the efficient reduction of disulfide bonds in lysozyme by tris(2-carboxyethyl)phosphine (TCEP) initiated rapid protein unfolding, followed by the formation of oligomers (with an average diameter of 30~50 nm) through the assembly of partially unfolded protein monomers, which were then enriched at the air/water interface to afford the nanofilm, driven by interfacial Gibbs free energy minimization.<sup>5,60–63</sup> Based on this mechanism and the above-mentioned evidence, it was reasonably inferred that after efficient reduction of the disulfide bonds of lysozyme by Sn<sup>2+</sup>, unfolded protein monomers assembled to form amyloid-like oligomers that were then aggregated at the air/water interface, as supported by the aforementioned AFM and TEM evidence (Figure 1d,e). With droplet flattening, the oligomer nanoparticles gradually migrated from the droplet periphery to the top flat plane of the droplet to form the hybrid film driven by the interfacial Gibbs free energy minimization (Figure 1a). Such depletion of the oligomer nanoparticles from the droplet periphery resulted in the increase of the surface tension of the droplet, as reflected by the increase of the water contact angle (WCA) with the flattening process proceeding (Figure 3e). The droplet flattening by the hybrid film was assisted by reducing the interfacial tension of a liquid droplet during the hybrid film formation,<sup>64</sup> and the stable presence of the droplet facet further indicated that the mechanical strength of the film was strong enough to overcome the lateral peeling from the surface tension at the air/water interface.<sup>65</sup> The protein hybrid film was then subjected to the nanoindentation analysis (Figure 3f), in which the Young's elastic modulus and the hardness of the hybrid film were measured to be 0.2 and 0.02 GPa, respectively.

The content of Sn in the hybrid film was further measured by thermogravimetric (TG) analysis (Figure 4a). At a given condition, a 60% weight loss due to the decomposition of organic compounds occurred at 570 °C for the hybrid film, so that the content of Sn in the hybrid film, as the remaining weight after the decomposition of organic structures, could be measured properly. Based on the TG characterization, a series of hybrid films containing different contents of Sn could be obtained by changing the concentration of Sn at the beginning of the reaction (Figure 4b). It could be seen that by increasing the concentration of Sn at the beginning of the reaction from 0.008 to 0.16 M, the time to form the visible hybrid film was shortened effectively from 120 min to 40 s, and meanwhile, the final Sn content in the hybrid film was elevated from 18% to 40%. Based on this measurement, the molar ratio of Sn to S in

the hybrid film was further analyzed at approximately 2:1–4:1, and this ratio indicated that the possible composition of the cluster formed in the hybrid film was  $-S-Sn(II)_x-S-$  ( $x = 4-8$ ). The hybrid film presented easy transfer and robust adhesion onto a variety of substrates because of the characteristic self-adhesive property of amyloid-like protein aggregation in the hybrid film.<sup>53</sup> Previously, we demonstrated that such robust interfacial adhesion was attributed to a multiplex binding model of amyloid-like protein aggregation with substrates.<sup>53</sup> As characterized by the WCA, several substrates including glass, indium tin oxide (ITO), polyethylene terephthalate (PET), and silicon (Si) exhibited nearly consistent WCA after their surfaces were coated by the hybrid film (Figure 4c). The AFM measurements of these modified substrates showed a clear morphology of the hybrid film being composed of an aggregation of oligomer nanoparticles (Figure S15). The adhesion between the film and the substrate was strong enough to pass through the mechanical peeling of 3 M Scotch adhesive tape and ultrasonic washing, respectively (Figure 4d, Figure S16). The film adhered onto the substrate also showed robustness in organic solvents or pH range of 2–13, showing unaffected original surface morphology in these harsh environments (Figure S17). The good robustness of the film was also contributed by the stabilization effect of Sn<sup>2+</sup> on the amyloid-like aggregation, based on the binding of Sn<sup>2+</sup> to Cys residues. For instance, the amyloid-like hybrid film doped with Sn was stable in the buffer of vitamin C that had the capability to specifically degrade the pure amyloid-like aggregation (without Sn doping) (Figure S18, movie S2, and movie S3).<sup>66</sup> The 2D film was formed not only at the air/water interface but also at the solid/liquid interface (*e.g.*, the outer surface of a 3D-printed resin object), indicating the applicability of this method to modify a scaffold with complex shapes (Figure S19). Due to the photosensitivity of the amide bonds of the protein in the hybrid film,<sup>5</sup> the film coated onto a substrate could easily form a micropattern by a photomask-controlled UV exposure, reflecting an ability to produce site-selective micropatterning on solid surfaces (Figure 4e). Interestingly, the self-recovery features of the hybrid film were also observed. When using a pipet tip to completely destroy the hybrid film floating at the air/water interface of the reactant solution, it was observed that the film could be quickly (within a few minutes) reformed at the air/water interface (movie S4, Figure S20), and this process was reversibly manipulated for many times. This process indicated that the Sn-triggered assembly of protein oligomer nanoparticles was self-recoverable, which might be ascribed to the dynamically reversible assembly of oligomer nanoparticles at the air/water interface. The introduction of tin ions into the hybrid film further imparted this proteinaceous material with multiple functions. A wide spectrum of antimicrobial capabilities with a 99% killing ratio toward *E. coli*, *S. aureus*, and *C. albicans* microbes were detected on the film, reflecting the benefit of this material for biomedical applications (Figure 4g). The possible mechanism for the antibacterial activity of the Sn/Lys hybrid toward Gram-positive/negative and fungi film may be explained as follows. First, the Sn/Lys hybrid film surface presented an enrichment of Sn-based clusters that facilitated the perturbation of the microbial cell walls or ROS generation and finally led to the death of microbes.<sup>67–69</sup> Second, the perturbation of the cell walls of microbes could be also caused by the increased cationic charge units from tin ions and lysozyme (the isoelectric point of lysozyme is 11), which

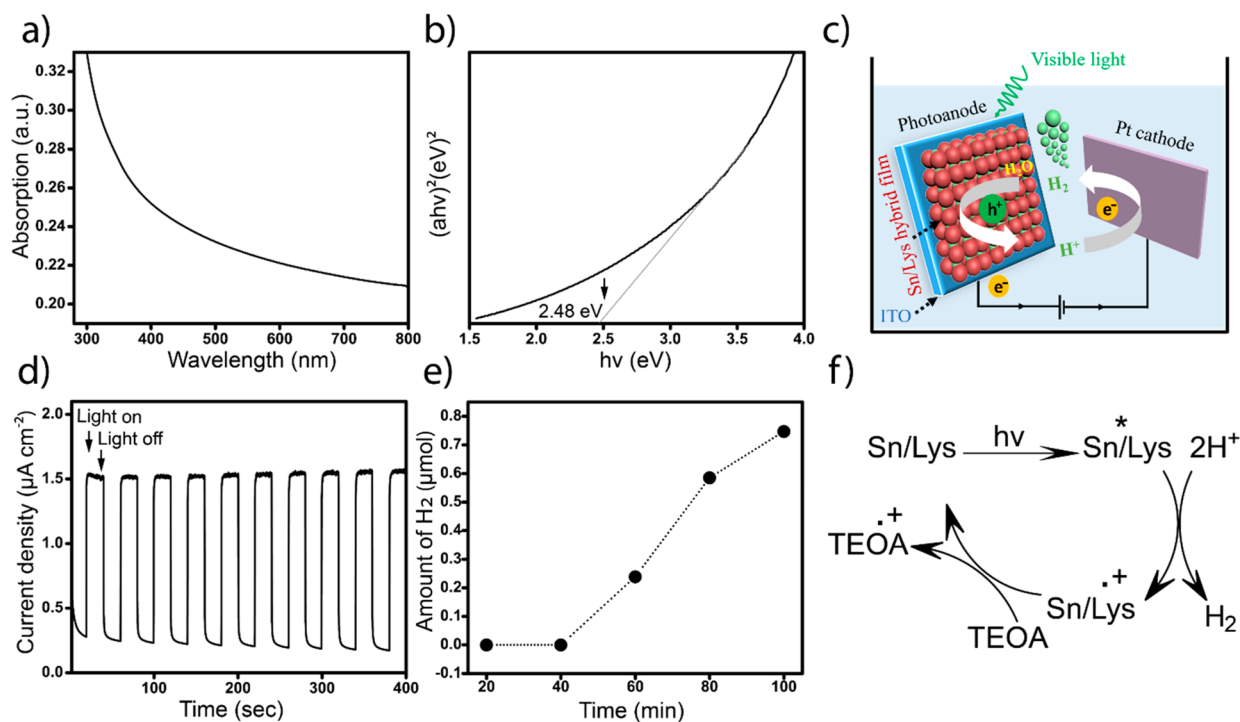


**Figure 5.** Optical properties and photocatalytic performance of the Sn/Lys hybrid film. (a, b) UV–vis diffuse reflectance spectra and optical band gap ( $E_g$ ) of the Sn/Lys hybrid film. (c) Schematic illustration showing the device for hydrogen generation using the Sn/Lys hybrid film as the coating on the photoanode. (d, e) Photocurrent (d) and amount of  $H_2$  (e) produced by the photocatalytic hydrogen reduction from the hybrid film as functions of the on/off switching of the light and the reaction time. (f) Proposed mechanism of hydrogen generation using the Sn/Lys hybrid film as a photocatalyst.

strengthened the electrostatic binding to negatively charged microbial membranes. Third, the existence of hydrophobic amino acid residues (e.g., Trp) arising from lysozyme on the protein hybrid film surface could induce an enhanced perturbation on the cell lipid membrane, which promoted the killing efficacy on microbes.<sup>70–72</sup> Lastly, the hydrophobic perturbation on cell walls of microbes to improve microbial killing performance could be further assisted by polymeric form of proteins.<sup>73,74</sup> The cytotoxicity measurement of this material also indicated that the hybrid film was biocompatible without detectable toxicity on mammalian cells (Figure S21). This result is reasonable since our previous study suggested the negligible cytotoxicity of amyloid-like aggregations of lysozymes<sup>75,76</sup> and the Sn contained in the hybrid film is a natural metal element with low cytotoxicity. Actually, the low toxicity of Sn also ensures its wide use in food containers and packaging, in which the anodic sacrifice of Sn plates is often utilized to electrochemically protect the base metal (iron) in tin-plated food cans.<sup>77</sup>

We further discovered the catalytic properties of the hybrid film. Despite the immense processing of MPs to date to catalyze many difficult reactions in nature, the development of artificial mimics with good biocatalytic properties is still an unmet challenge. In the present hybrid film, the coordination between Cys (S) and tin ( $Sn^{2+}$ ) led to the formation of  $-S-Sn(II)_x-S-$  clusters, which were potentially useful for photo/electrocatalytic applications due to the outstanding electronic, optical and photoelectronic properties of  $SnS_2$  with the band gap of 2.21–2.55 eV.<sup>29,46,78–80</sup> As shown in the UV–vis diffuse reflectance spectra (DRS) of the hybrid film (Figure 5a), the hybrid film showed certain absorption in the visible light

region, and the corresponding optical bandgap ( $E_g$ ) of the hybrid film was then calculated by the following formula<sup>81</sup>

$$\alpha hv = A(hv - E_g)^{1/2}$$

where  $\alpha$ ,  $hv$ ,  $A$ , and  $E_g$  represent the absorption coefficient, the photon energy, a constant, and the optical band gap energy, respectively. By extrapolating the linear portion of the curve  $(\alpha hv)^2$  vs  $(hv)$  to  $\alpha = 0$  in the UV–vis DRS (Figure 5b), the  $E_g$  value of the Sn/Lys hybrid film was estimated to be approximately 2.48 eV, which was in good agreement with previous reports.<sup>81</sup> The  $E_g$  value of the hybrid film suggested that it is a potential visible-light-responding material for photocatalytic applications. To confirm the generation of photogenerated charges over the hybrid film and to verify the photocatalytic activity of the hybrid film, we then probed the function of the hybrid film for photoelectrochemical (PEC) performance using a three-electrode setup in 0.2 M  $Na_2SO_4$  (Figure 5c). The photocurrent of the hybrid film was tested at open-circuit current under visible-light irradiation ( $\lambda > 420$  nm), and the light was switched on/off every 20 s. With the hybrid film as the coating on the photoanode and Pt as the cathode, a device was designed to present long-term photocurrent stability, with its response at a current density of  $1.55 \mu A cm^{-2}$ , and no apparent photocurrent degradation could be observed within the duration time of  $\sim 400$  s (Figure 5d). This value was much higher than that reported for bulk  $SnS_2$ .<sup>82</sup> To further verify the photocatalytic activities, the  $H_2$  generation reaction was carried out in aqueous solution with triethanolamine (TEOA) (15 vol %) as the sacrificial agent under visible light ( $>420$  nm). The rate of hydrogen evolution from this device was then measured, in which a total amount of  $0.75 \mu mol H_2$  was produced at  $t = 100$  min under visible-light

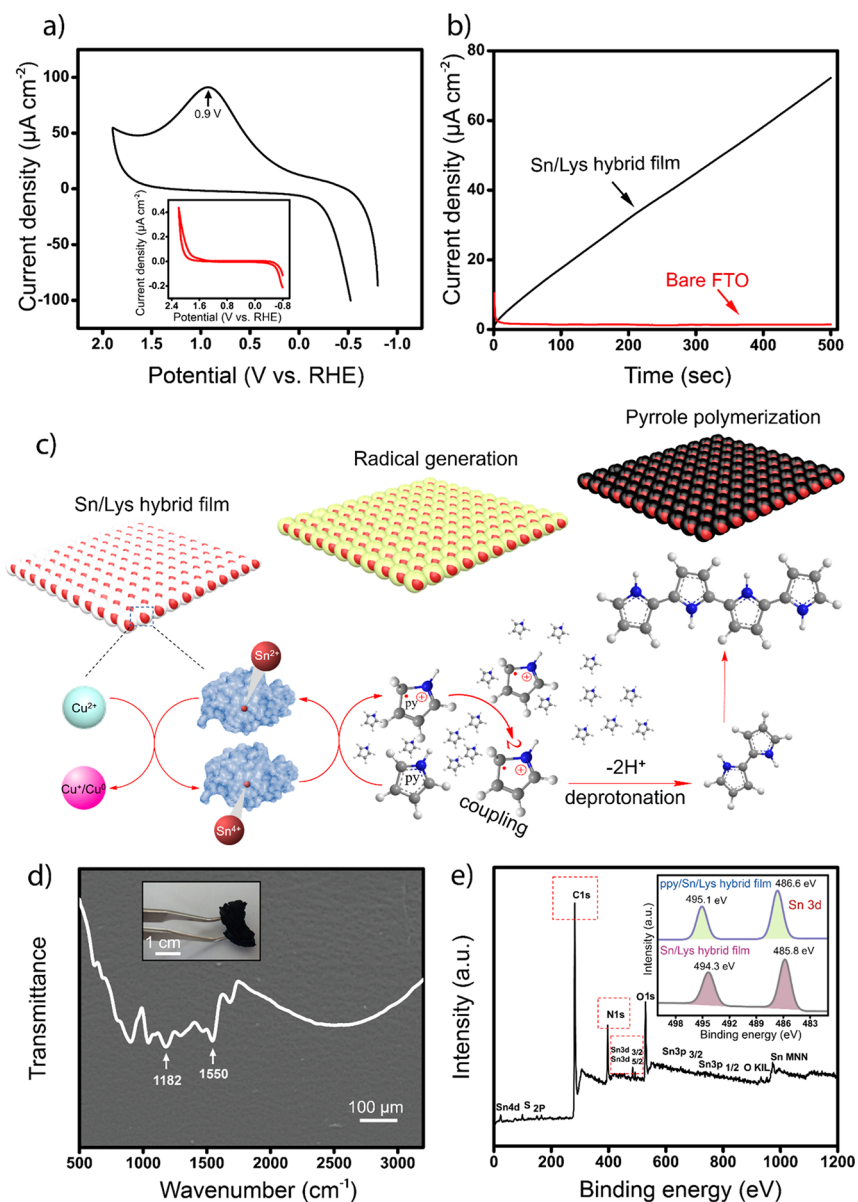


**Figure 6.** Electrochemical performance of the Sn/Lys hybrid film. (a) Cyclic voltammetry (CV) curve of the Sn/Lys hybrid film on FTO glass in 0.2 M  $\text{Na}_2\text{SO}_4$  electrolyte at a scan rate of  $100 \text{ mV s}^{-1}$ . The oxidation peak associated with the radical generated from  $-\text{S}-\text{Sn}(\text{II})_x-\text{S}-$  clusters in the hybrid film appeared at a potential of 0.9 V *versus* RHE. Inset in (a) shows the CV test of the bare FTO substrate. (b) Current density of the Sn/Lys hybrid film-coated FTO (black) and bare FTO (red) during bulk electrolysis at 0.9 V in 0.2 M  $\text{Na}_2\text{SO}_4$  containing 50 mM pyrrole. (c) Schematic illustration of  $\text{Cu}^{2+}$ -driven pyrrole polymerization on the Sn/Lys hybrid film. (d) FT-IR spectra of the ppy/Sn/Lys hybrid composite film prepared by  $\text{Cu}^{2+}$ -driven pyrrole polymerization. The corresponding insets in (d) showed the SEM and photograph images of the polypyrrole/Sn/Lys hybrid composite film, respectively. (e) XPS spectra of the polypyrrole/Sn/Lys hybrid composite film, with the inset showing the valence change of tin ions in the hybrid film before and after the polymerization of pyrrole.

irradiation (Figure 5e). The proposed mechanism of the hybrid film acting as a photocatalyst is shown in Figure 5f. Under visible-light irradiation, the electrons were excited from  $-\text{S}-\text{Sn}(\text{II})_x-\text{S}-$  clusters in the hybrid film to produce electron/hole pairs ( $\text{Sn}^*/\text{Lys}$ ) due to the absorption of photons with a higher photoenergy than the band gap of the  $-\text{S}-\text{Sn}(\text{II})_x-\text{S}-$  clusters in the hybrid film, followed by attaining the charge-separated state ( $\text{Sn}^{*+}/\text{Lys}$ ) and migration to the photocatalyst surface for  $\text{H}^+$  reduction. Meanwhile, TEOA, as an electron donor in the solution would recover the excited state of Sn/Lys.

To further explore the possibility of the hybrid film as a biomimic catalytic scaffold, the oxidative polymerization of

pyrrole was chosen as a model reaction. For most approaches to polypyrrole synthesis, electrochemical oxidation or the addition of oxidants is required to achieve polymerization.<sup>83–85</sup> Herein, we propose an alternative approach to enhance the chemical reaction that mimics native enzymes by utilizing  $-\text{S}-\text{Sn}(\text{II})_x-\text{S}-$  clusters in the hybrid film. In nature, the tyrosyl radical has been well researched as an efficient electron-transfer mechanism in biological systems. Recently, much attention has focused on tyrosyl radicals from designed synthetic peptide scaffolds as biocatalytic triggers for the polymerization of pyrrole.<sup>65</sup> Interestingly, we found that an oxidized peak was easily generated from  $-\text{S}-\text{Sn}(\text{II})_x-\text{S}-$  clusters in the hybrid film by applying a potential of 0.9 V (Figure 6a), which was not

detectable in the pure phase-transited lysozyme film without Sn doping,<sup>5</sup> as evidenced by the cyclic voltammetry (CV) curves (Figure 6a, Figure S22). This peak reflected the electricity-induced oxidation of Sn<sup>2+</sup> to Sn<sup>4+</sup>. To explore the possible use of this redox reaction in the protein hybrid film, the oxidative polymerization of pyrrole was explored as a model reaction. In general, polypyrrole can be significantly synthesized by applying a potential higher than 1.0 V or by using an oxidant, such as iron(III) chloride (FeCl<sub>3</sub>) or sodium persulfate (Na<sub>2</sub>S<sub>2</sub>O<sub>8</sub>). A potential lower than 1.0 V (*e.g.*, 0.9 V) would not drive obvious macroscopic polypyrrole deposition. Indeed, our experimental results also consistently confirmed that with the use of a potential at 0.9 V there was a negligible amount of polypyrrole deposition on a blank fluorine-doped tin oxide (FTO) substrate, with nearly unchanged zero-current density until the reaction end (Figure 6b). In contrast, a black polypyrrole film was deposited onto the Sn/Lys hybrid film-coated FTO substrate under a constant potential of 0.9 V, and the corresponding current density linearly increased with the time, attaining >70  $\mu\text{A}$  after 500 s (Figure 6b). This result implied that in this process the Sn<sup>4+</sup> formed *in situ* by the oxidation of Sn<sup>2+</sup> under electricity would then oxidize pyrrole to form a pyrrole radical, which then initiated the polymerization of pyrrole under a relatively low voltage.

On the basis of the electrochemically driven radical generation, we further designed an experiment to probe the hybrid film as a biomimetic artificial enzyme. In nature, galactose oxidase can generate radicals by a valence change of the copper ion (Cu<sup>2+</sup>) without applying any additional potential.<sup>86</sup> We then found that the  $-\text{S}-\text{Sn}(\text{II})_x-\text{S}-$  clusters in the hybrid film were also able to initiate the oxidized polymerization of pyrrole to form polypyrrole using Cu<sup>2+</sup> without applying any additional potential. A schematic of the polymerization reaction is shown in Figure 6c. First, Sn<sup>2+</sup> in the  $-\text{S}-\text{Sn}(\text{II})_x-\text{S}-$  clusters of the hybrid film could be oxidized by Cu<sup>2+</sup> to form Sn<sup>4+</sup> (electrochemical series: Sn > Cu), which subsequently oxidized the pyrrole monomer to form a pyrrole cationic radical. As a result, the oxidative polymerization of pyrrole was induced by the resultant radicals, which was clearly reflected by the black polypyrrole deposition formed on the hybrid film, finally affording a free-standing composite film of polypyrrole and protein (Figure 6d). The FT-IR bands at 1182 and 1550  $\text{cm}^{-1}$  were attributed to C–N and C=C backbone stretching of the polypyrrole ring, suggesting the successful polymerization of pyrrole in the presence of the Sn/Lys hybrid film (Figure 6d).<sup>87</sup> The significant variation in the binding energy of Sn<sub>3d</sub> from the XPS results on the film before and after initiating the polymerization of pyrrole further provided key evidence to support the proposed catalytic mechanism (Figure 6e). In comparison to Sn<sup>2+</sup> on the film before the polymerization, the valence state of Sn on the film after the reaction was shifted to a higher binding energy at 486.6 and 495.1 eV, which reflected a higher oxidation state of Sn resulting from the polymerized hybrid film. Furthermore, the Cu<sub>2p</sub> XPS spectrum on the polymerized composite film demonstrated the valence change of Cu<sup>2+</sup> to Cu<sup>0</sup>/Cu<sup>+</sup> after the polymerization reaction (Figure S23). The two binding peaks at 932.9 and 952.6 eV were assignable to Cu<sub>2p3/2</sub> and Cu<sub>2p1/2</sub> for Cu(0) and/or Cu(I), respectively.<sup>88</sup> The above valence change of Sn and Cu as revealed by XPS was consistent with the reaction pathway of Sn<sup>2+</sup> to Sn<sup>4+</sup> and of Cu<sup>2+</sup> to Cu<sup>0</sup>/Cu<sup>+</sup> proposed in the hypothesized mechanism. Previously, highly concentrated metals, *e.g.*, Cu<sup>2+</sup>, Fe<sup>2+</sup>, and

Zn<sup>2+</sup>, were found to be colocalized within A $\beta$  plaques to contribute to the change of A $\beta$  aggregation kinetics,<sup>89</sup> the stabilization of oligomer toxicity, and oxidative stress.<sup>90</sup> In this regard, our present results implied that the artificial regulation of nonmetalloproteins by tin ions could potentially create a class of metal–amyloid complex presenting beneficial catalytic and biocompatibility properties.<sup>91,92</sup>

## CONCLUSION

In summary, our results suggest a platform for the construction of functionally controllable 2D hybrid metal/protein nanostructures. The self-assembly faceting at the air/water interface highlights the role of Sn<sup>2+</sup> in amyloid-like protein packing and the importance of metal–protein clusters in organization behaviors. Our findings provide insight into obtaining self-assembled protein interfaces through dynamic curvature control and site-selective functionalization. The advantages of the present method include the uniformity of the film and the capabilities of large-scale deposition, room-temperature processing, and thickness control. The droplet faceting and resultant formation of the hybrid film are also expandable to other proteins, *e.g.*, bovine serum albumin (BSA),  $\beta$ -lactoglobulin, and insulin, which have structure features similar to those of lysozyme toward superfast amyloid-like protein assembly (Figures S24–S26, movie S5, movie S6, and movie S7).<sup>62</sup> The resultant material exhibits versatile functions that mimic the roles of native proteins including an integration of biomimic photocatalytic performance for hydrogen reduction and pyrrole polymerization, antimicrobial capability, biocompatibility, and robust interfacial adhesion onto virtually arbitrary material surfaces.

With its stable mechanical strength and self-recovering ability, we believe that our scalable and functionally extendable hybrid film represents not only a significant step in the bioinspired synthesis of enzyme mimetic catalyst but also the development of bioresource-based nanobiotechnology and synthetic biology. For instance, on the basis of recent work on cell surface engineering using amyloid-inspired protein coatings,<sup>93</sup> the present method may be potentially useful for tailoring living cells by arming them with photo-/electrocatalytic functions. With the aim of exploiting chemical and structural versatility of proteins as building blocks for biological materials and devices, we further expect that this strategy could be utilized in a variety of applications, such as floating scaffolds for cell culture, responsive vesicles for drug delivery, ion-selective membranes, 2D-ordered conducting polymers, elastic protein mimetics, and metalloprotein-based catalysts.

## EXPERIMENTAL METHODS

**Materials.** Lysozyme (hen egg white), bovine serum albumin (BSA), 8-anilino-1 naphthalenesulfonic (ANS), agarose, triton X-100, ALP assay kit, thioflavin-T (ThT), and phosphotungstic acid were purchased from Sigma-Aldrich. Pig insulin was purchased from Aladdin,  $\beta$ -lactoglobulin was purchased from Yuanyebio Co., Ltd., sodium chloride (NaCl), hydrochloric acid (HCl), and sodium hydroxide (NaOH) were purchased from Sinopharm Chemical Reagent Co., Ltd., and tin chloride (SnCl<sub>2</sub>), copper chloride (CuCl<sub>2</sub>), and pyrrole were purchased from Aladdin. Phosphate-buffered saline (PBS), (4-(2-hydroxyethyl)-1-piperazineethanesulfonic acid) (HEPES) buffer (pH = 7.2–7.4), and sodium diphenyl diazobis- $\alpha$ -naphthylamine-4-sulfonate (Congo red) were obtained from Solarbio. Triethanolamine (TEOA) was purchased from Guangdong Guanghua Sci-Tech Co., Ltd. *E. coli* (ATCC 8739), *S. aureus* (ATCC 29213), and *C. albicans* (ATCC 10231) were obtained

from the American Type Culture Collection (USA). The Cell Counting Kit-8 (CCK-8) was purchased from Beyotime Institute of Biotechnology. The adhesive tapes (Scotch Brand Tapes) were purchased from 3 M China. Indium tin oxide (ITO) coated glass plates, fluorine-doped tin oxide (FTO) coated glass plates, and the super flat glass (the grade for electronic industry) were obtained from NanBo Co., Ltd. High-quality commercial poly(ethylene terephthalate) (PET) foil, ITO-coated glass, and FTO-coated glass were subjected to ultrasonic cleaning with acetone and ethanol and then dried under a stream of nitrogen. Ultrapure water was used in all experiments and was supplied by Milli-Q Advantage A10 (Millipore, USA). The silicon wafer was purchased from Resemi Co., Ltd., and cleaned in piranha solution (3:1 v/v) mixture of sulfuric acid (H<sub>2</sub>SO<sub>4</sub>) and hydrogen peroxide (H<sub>2</sub>O<sub>2</sub>) at 80 °C for 8 h. (*Caution: Piranha solution reacts violently with organic materials; it must be handled with extreme care, followed by copious rinsing with ultrapure water and dried under a nitrogen stream.*) The copper grids covered with a pure carbon film (230 mesh) were purchased from Beijing Xinxing Brain Tech. Co., Ltd.

**Preparation of the Sn/Lys Hybrid Protein Film.** The Sn/Lys hybrid film was easily prepared by quick mixing of 1 mL of lysozyme (typically between 10 and 20 mg/mL in 10 mM HEPES buffer) with 30  $\mu$ L of 0.1 M SnCl<sub>2</sub> (pH 1.8) at room temperature. Alternatively, 0.08 g of SnCl<sub>2</sub> powder was added into 10 mL of lysozyme (typically between 10 and 20 mg/mL in 10 mM HEPES buffer) with quick stirring for about 2 min at room temperature, and then the final pH of the resulting solution was adjusted to 1.8 using HCl (the low pH ensured the completely soluble state of SnCl<sub>2</sub>; otherwise, SnCl<sub>2</sub> would easily hydrolyze to form insoluble precipitates at a pH > 2). After that, the resulting solution was dropped on different substrates such as PET, silicon, ITO, or FTO glass as well as a Petri dish. Then the Sn/Lys hybrid film could be clearly formed at the air/liquid interface within 5 min. The corresponding facet at air/water interface could be observed typically in 1–5 min.

**Evaluation of the Adhesion and Chemical Stability of the Sn/Lys Hybrid Film on a Substrate.** First, the Sn/Lys hybrid film was prepared by mixing 1 mL of lysozyme (20 mg/mL in 10 mM HEPES buffer) with 30  $\mu$ L of 0.1 M SnCl<sub>2</sub> (pH 1.8), and the resultant hybrid film was then floated on the surface of the ultrapure water which then readily transferred onto silicon, glass, or PET substrates. The transferred Sn/Lys hybrid film was then rinsed with ultrapure water to remove the salt and then was dried by nitrogen. For the chemical stability test, the Sn/Lys hybrid film-coated substrate was immersed into ethanol, hexane, petroleum ether, HCl aqueous (pH 2, 3), or NaOH aqueous solution (pH 9, 13) for 30 min, respectively. For the adhesion test, the hybrid film coating on a substrate was subjected to the 3 M Scotch adhesive tape peeling three times, in which a small piece of Scotch adhesive tape was pressed firmly on the Sn/Lys hybrid film coated substrate and then removed quickly.

**Photolithography on the Sn/Lys Hybrid Film.** Typically, positive patterning on the hybrid film was carried out by exposing the hybrid film under UV light at 12000  $\mu$ w/cm<sup>2</sup> (mainly 365 nm wavelength) from the topside (a high-pressure mercury lamp, 1000 W) for 1 h, with a control of a photomask. After UV exposure, these irradiated samples were directly developed in ultrapure water for 30 s (to rinse the degraded molecular species) and dried by a nitrogen gas gun.

**Cell Viability Assay.**<sup>94</sup> The Sn/Lys hybrid film-coated Ti and blank Ti substrates were sterilized with ultraviolet light exposure and 70% ethanol soaking for 2 h. In order to evaluate the potential cell viability of the Sn/Lys hybrid film against rat bone marrow mesenchymal stem cells (rBMSCs), the samples were then soaked in DMEM for 24 h to obtain the extracts for rBMSCs culture. rBMSCs were seeded in 96-well plates at  $1 \times 10^4$  cells/cm<sup>2</sup> and incubated with extracts at 37 °C in a humidified atmosphere with 5% CO<sub>2</sub> for 7 days using DMEM as control. The medium was refreshed every other day. Cell proliferation was analyzed using a Cell Counting Kit-8 (CCK-8). After culture for 3, 5, and 7 days, 100  $\mu$ L of new medium and 10  $\mu$ L of CCK-8 solution were added to each well of a 96-well plate and then incubated at 37 °C in 5% CO<sub>2</sub> for 4 h. Finally,

the OD value of the incubated solution was measured with a spectrophotometric microplate reader (Bio-Rad 680, USA) at 450 nm.

**Alkaline Phosphatase Activity (ALP Activity).**<sup>95</sup> ALP activity was an indicator of osteoblastic differentiation of rBMSCs. For this goal, the ALP activity of the Sn/Lys hybrid film-coated Ti substrate and blank Ti substrate was determined using an ALP assay kit according to the manufacturer's instructions. After the cells or cell/matrix complexes were incubated in osteogenic inductive medium for 3, 5, and 7 days, they were retrieved from trans well chambers or culture plates and rinsed with PBS three times. Then the cells were lysated by cell lysis buffer (10 mM Tris-HCl, containing 2 mM NaCl and 1% Triton X-100, pH 7.5). After that, culture supernatants (30  $\mu$ L) were collected from each well. Samples were put in alkaline buffer and added with 50  $\mu$ L of pNPP solution. The reaction was stopped with 150  $\mu$ L of chromogenic agent incubated in ALP detection buffer for 15 min at 37 °C. The absorbance at 520 nm was measured on a microreader (Bio-Rad 680). The ALP activities were normalized to the total protein content determined by using the BCA assay kit (Thermo) according to the manufacturer's instructions.

**Photocatalytic Performance of the Sn/Lys Hybrid Film.** The photocatalytic activity for hydrogen evolution under visible light was performed in a closed gas-recirculation system equipped with a top-irradiation (quartz glass) Pyrex cell. Typically, 0.03 g of Sn/Lys hybrid film sample was dispersed into a solution mixture of 10 mL of triethanolamine (TEOA) as a sacrificial agent and 90 mL of distilled water. The resulting dispersion was then evacuated for 30 min to remove air prior to irradiation under a 300 W xenon lamp (PLS-SXE300UV, Perfectlight) equipped with a cutoff filter ( $\lambda > 420$  nm). The evolved hydrogen gas was circulated with a gas pump and quantified at a regular interval by gas chromatography (Shiweipx GC7806) with thermal conductivity detector (TCD). The photoelectrochemical measurements of the Sn/Lys hybrid film were carried out in a conventional three-electrode cell system using a CHI600E electrochemical analyzer (Chenhua Instruments Co., Shanghai) in which the Sn/Lys hybrid film was transferred onto ITO-coated glass and used directly as the working electrode. A Pt wire and Ag/AgCl were used as counter and reference electrodes, respectively. An aqueous solution containing Na<sub>2</sub>SO<sub>4</sub> (0.2 M) was used as the electrolyte. The photoelectrode was exposed under visible-light irradiation (300 W Xe lamp,  $\lambda > 420$  nm), and the photocurrent density was measured at a scan rate of 100 mV s<sup>-1</sup>.

**Electrocatalytic Performance of the Sn/Lys Hybrid Film.** To examine the electrocatalytic performance of the Sn/Lys hybrid film, 5 mL of lysozyme (20 mg/mL in 10 mM HEPES buffer) was mixed with 1 mL of 0.1 M SnCl<sub>2</sub> (pH 1.8) at room temperature, in which the resultant hybrid film was floating on a pure water surface and then transferred onto FTO-coated glass and dried under a stream of nitrogen. All electrochemical measurements were performed in a three-electrode configuration using the Sn/Lys hybrid film-coated FTO as the working electrode, Pt wire as a counter electrode, and Ag/AgCl as a reference electrode. The working electrode was performed using cyclic voltammetry. The electrode was cycled between -1 and 1.8 V versus Ag/AgCl in 0.2 M Na<sub>2</sub>SO<sub>4</sub> at a scan rate of 100 mV s<sup>-1</sup>. All electrochemical measurements were carried out in 0.2 M Na<sub>2</sub>SO<sub>4</sub> (pH 5.3) solutions, and the measured potentials vs the saturated Ag/AgCl reference electrode were converted to the reversible hydrogen electrode (RHE) using the Nernst equation<sup>96</sup>

$$E_{\text{RHE}} = E_{\text{Ag/AgCl}} + 0.059\text{pH} + E^{\circ}_{\text{Ag/AgCl}}$$

where  $E_{\text{RHE}}$  is the converted potential vs RHE,  $E_{\text{Ag/AgCl}}$  is the measured potential against the saturated Ag/AgCl reference electrode, and  $E^{\circ}_{\text{Ag/AgCl}}$  is the standard potential of Ag/AgCl at 25 °C, which is 0.1976 V. For the experiment without any additional potential applied, typically, 5 mL of lysozyme buffer (20 mg/mL in 10 mM HEPES buffer) was mixed with 0.8 mL of 0.1 M SnCl<sub>2</sub> solution (pH 1.8) at room temperature. After that, the resulting Sn/Lys hybrid film was incubated in 50 mM Cu(II) chloride solution and then exposed to the vapor of 50 mM of monomer pyrrole solution for 30 h at room temperature, in which a black polypyrrole film was finally formed on

the hybrid film to afford a free-standing composite film of polypyrrole and protein. The resulting free-standing polypyrrole/Sn/Lys hybrid film was then taken out, washed with ultrapure water, and dried under vacuum.

**Transmission Electron Microscopy (TEM).** For TEM analysis, the Sn/Lys hybrid film was carefully placed on a 230-mesh carbon-coated copper grids, negatively stained with 3% (w/v) of phosphotungstic acid aqueous solution and air-dried for TEM measurements. The grids were checked using FEI Tecnai G2 F20 field TEM with an acceleration voltage of 200 kV.

**Atomic Force Microscopy (AFM).** For AFM images, the Sn/Lys hybrid film was transferred onto a clean silicon substrate. After that, the adhered film on the silicon substrate was rinsed with ultrapure water to remove the salt and then dried by nitrogen. AFM was performed by CSPM 5500 (MultiMode, NanoScope IV from Benyuan, Inc., China), and the silicon cantilevers with resonance frequencies of  $f_0 = 300$  kHz and spring constants of  $k = 40$  N/m were used. The root-mean-square (RMS) of the resulting film was analyzed by CSPM Imager 4.7 software.

**X-ray Photoelectron Spectroscopy (XPS).** XPS of native lysozyme (powder) and the Sn/Lys hybrid film was analyzed with AXIS ULTRA from Kratos Analytical, Ltd., and the binding energies were calibrated by setting the C 1s peak at 284.5 eV.

**Fourier Transform Infrared (FT-IR) Spectroscopy.** FT-IR spectra of native lysozyme (powder) and the Sn/Lys hybrid film were analyzed using a Vertex 70v spectrometer (Bruker Inc., Germany) with the spectra obtained between 400 and 4000  $\text{cm}^{-1}$  using an Alpha-T spectrometer (Bruker).

**Water Contact Angle (WCA).** After 12  $\mu\text{L}$  of the reaction solution (the mixture of lysozyme and tin chloride) was dropped on the pristine or the hybrid film-coated glass, ITO, PET, or Si substrates, WCA measurements and side-view recording of the faceting process on the droplet surface were performed by an OCA 20 (Dataphysics, Germany) on these substrates.

**Confocal Laser Scanning Microscopy (Fluorescence Imaging).** Briefly, 200  $\mu\text{L}$  of thioflavin-T (ThT) solution (100  $\mu\text{M}$ ) was added to 3 mL of lysozyme buffer (20 mg/mL in 10 mM HEPES buffer). After the mixture was incubated in the dark for 5 min, 300  $\mu\text{L}$  of tin chloride solution (0.1 M) was added, and then the resulting stained hybrid film was deposited on glass slide and covered with a glass coverslip. The ThT-bound Sn/Lys hybrid film was then subjected to fluorescence imaging analysis with excitation at 458 nm. The confocal microscopy images were taken on an Olympus confocal laser scanning microscopy microscope (FV1200). As the control experiment, the control experiment without ThT added under the same conditions was subjected to fluorescence imaging.

**ThT Staining.** The fluorescence spectrum was collected using an FLS-920 fluorescence spectrophotometer (Edinburgh Instruments). The formation of a  $\beta$ -sheet in the presence of tin ions was monitored using ThT fluorescence.<sup>97</sup> Briefly, 100  $\mu\text{L}$  of ThT solution (100  $\mu\text{M}$ ) was added to a quartz cuvette containing 2 mL of freshly prepared lysozyme (17 mg/mL) and incubated in the cuvette for 10 min, and then 800  $\mu\text{L}$  of 0.1 M  $\text{SnCl}_2$  (pH 1.8) was added to the cuvette. As the control experiment, 100  $\mu\text{L}$  of ThT solution was added to a quartz cuvette containing 2 mL freshly prepared lysozyme buffer (17 mg/mL) and incubated in the cuvette for 10 min. The stained samples were then subjected to fluorescence spectrum recording, and the emission at 486 nm was measured as a function of time using excitation at 450 nm.

**ANS Binding Assay.** 1-Anilinonaphthalene 8-sulfonate (ANS) as a fluorescent probe is commonly used to detect the exposure of hydrophobic residues<sup>98</sup> of lysozyme in the presence of tin ions. A 2 mL portion of lysozyme solution (17 mg/mL) was mixed with 300  $\mu\text{L}$  of ANS (100  $\mu\text{M}$ ) and placed in the dark at room temperature for 30 min, and 500  $\mu\text{L}$  of tin chloride was then added. As the control experiment, 2 mL of lysozyme (17 mg/mL) was mixed with 300  $\mu\text{L}$  of ANS and placed in the dark at room temperature for 30 min. Fluorescence analysis on the stained samples was then performed with a FLS-920 fluorescence spectrophotometer (Edinburgh Instruments) by measuring emission spectra at 480 nm with excitation at 355 nm.

**Congo Red Staining.** The Sn/Lys hybrid film was immersed in 20 mL of 1 mg/mL Congo red solution at room temperature for 1 h. The stained hybrid film was then taken out and washed with ultrapure water for three times.

**Raman Spectroscopy.** Raman spectra of native lysozyme (powder) and the Sn/Lys hybrid film were analyzed with a Renishaw Raman spectrometer *via* Reflex (wavelength laser 532 nm, power = 250 mW). The scanned wavenumbers ranged between 100 and 3200  $\text{cm}^{-1}$ .

**Scanning Electron Microscopy (SEM).** Scanning electron microscopy images of the Sn/Lys hybrid films were collected by using FEI Quanta 200 and Hitachi TM3030. The cross-sectional analysis of the Sn/Lys hybrid film was wetting-off in liquid nitrogen and obtained using field emission SEM (FE-SEM), SU8020 (Hitachi).

**Optical Microscopy.** Optical microscopic observations of the Sn/Lys hybrid films and the faceting process were monitored over time by using Nikon Ti-U (Tokyo, Japan).

**Thermogravimetric Analysis (TGA).** Thermogravimetry analysis were carried out on a thermogravimetric analyzer (Q50 TGA, TA).

## ASSOCIATED CONTENT

### Supporting Information

The Supporting Information is available free of charge on the ACS Publications website at DOI: 10.1021/acsnano.9b01392.

Figures S1–S26, captions for movies S1–S7, and supplementary references (PDF)

Faceting on the reaction droplet due to the formation of the Sn/Lys hybrid film on the top of the droplet (AVI)

Effect of vitamin C on the Sn/Lys hybrid film (AVI)

Effect of vitamin C on the pure phase-transited lysozyme film without Sn doping (AVI)

Self-recovering ability of the Sn/Lys hybrid film (AVI)

Formation of the Sn/BSA hybrid film on the top of the droplet (AVI)

Formation of the Sn/Insulin hybrid film on the top of the droplet (AVI)

Formation of the Sn/ $\beta$ -lactoglobulin hybrid film on the top of the droplet (AVI)

## AUTHOR INFORMATION

### Corresponding Authors

\*E-mail: yangpeng@snnu.edu.cn.

\*E-mail: guquan@snnu.edu.cn.

### ORCID

Quan Gu: 0000-0002-9194-1994

Peng Yang: 0000-0002-0463-1024

### Notes

The authors declare no competing financial interest.

## ACKNOWLEDGMENTS

P.Y. and Q.G. acknowledge funding from the National Natural Science Foundation of China (Nos. 51673112, 21875132, 21872089, and 21503127), the 111 Project (No. B14041), the Natural Science Basic Research Plan in Shaanxi Province of China (No. 2017JM2008), the Fundamental Research Funds for the Central Universities (Nos. GK201801003, 2017CBY004, GK201903038), and the Open Project of the State Key Laboratory of Supramolecular Structure and Materials (No. sklssm2019032).

## REFERENCES

- (1) Jiang, T.; Xu, C.; Liu, Y.; Liu, Z.; Wall, J. S.; Zuo, X.; Lian, T.; Salaita, K.; Ni, C.; Pochan, D. Structurally Defined Nanoscale Sheets from Self-Assembly of Collagen-Mimetic Peptides. *J. Am. Chem. Soc.* **2014**, *136*, 4300–4308.
- (2) Nam, K. T.; Shelby, S. A.; Choi, P. H.; Marciel, A. B.; Chen, R.; Tan, L.; Chu, T. K.; Mesch, R. A.; Lee, B.-C.; Connolly, M. D. Free-Floating Ultrathin Two-Dimensional Crystals from Sequence-Specific Peptoid Polymers. *Nat. Mater.* **2010**, *9*, 454.
- (3) Zhang, J.; Zheng, F.; Grigoryan, G. Design and Designability of Protein-Based Assemblies. *Curr. Opin. Struct. Biol.* **2014**, *27*, 79–86.
- (4) Luo, Q.; Hou, C.; Bai, Y.; Wang, R.; Liu, J. Protein Assembly: Versatile Approaches to Construct Highly Ordered Nanostructures. *Chem. Rev.* **2016**, *116*, 13571–13632.
- (5) Wang, D.; Ha, Y.; Gu, J.; Li, Q.; Zhang, L.; Yang, P. 2D Protein Supramolecular Nanofilm with Exceptionally Large Area and Emergent Functions. *Adv. Mater.* **2016**, *28*, 7414–7423.
- (6) Lu, Y.; Berry, S. M.; Pfister, T. D. Engineering Novel Metalloproteins: Design of Metal-Binding Sites into Native Protein Scaffolds. *Chem. Rev.* **2001**, *101*, 3047–3080.
- (7) Manesis, A. C.; O'Connor, M. J.; Schneider, C. R.; Shafaat, H. S. Multielectron Chemistry within a Model Nickel Metalloprotein: Mechanistic Implications for Acetyl-CoA Synthase. *J. Am. Chem. Soc.* **2017**, *139*, 10328–10338.
- (8) Zastrow, M. L.; Pecoraro, V. L. Designing Hydrolytic Zinc Metalloenzymes. *Biochemistry* **2014**, *53*, 957–978.
- (9) Bonanni, B.; Andolfi, L.; Bizzarri, A. R.; Cannistraro, S. Functional Metalloproteins Integrated with Conductive Substrates: Detecting Single Molecules and Sensing Individual Recognition Events. *J. Phys. Chem. B* **2007**, *111*, 5062–5075.
- (10) Lee, T.; Kim, S. U.; Min, J.; Choi, J. W. Multilevel Biomemory Device Consisting of Recombinant Azurin/Cytochrome c. *Adv. Mater.* **2010**, *22*, 510–514.
- (11) Jensen, P. S.; Engelbrekt, C.; Sørensen, K. H.; Zhang, J.; Chi, Q.; Ulstrup, J. Au-Biocompatible Metallic Nanostructures in Metalloprotein Electrochemistry and Electrocatalysis. *J. Mater. Chem.* **2012**, *22*, 13877–13882.
- (12) Barker, P. D. Designing Redox Metalloproteins from Bottom-Up and Top-Down Perspectives. *Curr. Opin. Struct. Biol.* **2003**, *13*, 490–499.
- (13) Lu, Y.; Yeung, N.; Sieracki, N.; Marshall, N. M. Design of Functional Metalloproteins. *Nature* **2009**, *460*, 855–862.
- (14) Ulas, G.; Lemmin, T.; Wu, Y.; Gassner, G. T.; DeGrado, W. F. Designed Metalloprotein Stabilizes a Semiquinone Radical. *Nat. Chem.* **2016**, *8*, 354–359.
- (15) Petrik, I. D.; Liu, J.; Lu, Y. Metalloenzyme Design and Engineering through Strategic Modifications of Native Protein Scaffolds. *Curr. Opin. Chem. Biol.* **2014**, *19*, 67–75.
- (16) Parmar, A. S.; Pike, D.; Nanda, V. Computational Design of Metalloproteins. *Methods Mol. Biol.* **2014**, *1216*, 233–249.
- (17) Khare, S. D.; Kipnis, Y.; Takeuchi, R.; Ashani, Y.; Goldsmith, M.; Song, Y.; Gallaher, J. L.; Stoddard, B. L.; Tawfik, D. S.; Baker, D. Computational Redesign of a Mononuclear Zinc Metalloenzyme for Organophosphate Hydrolysis. *Nat. Chem. Biol.* **2012**, *8*, 294–300.
- (18) Tolman, W. B.; Spencer, D. J. New Advances in Ligand Design for Synthetic Modeling of Metalloprotein Active Sites. *Curr. Opin. Chem. Biol.* **2001**, *5*, 188–195.
- (19) Chino, M.; Maglio, O.; Natri, F.; Pavone, V.; DeGrado, W. F.; Lombardi, A. Artificial Diiron Enzymes with a De Novo Designed Four-Helix Bundle Structure. *Eur. J. Inorg. Chem.* **2015**, *2015*, 3371–3390.
- (20) Lu, Y. Metalloprotein and Metallo-DNA/RNAzyme Design: Current Approaches, Success Measures, and Future Challenges. *Inorg. Chem.* **2006**, *45*, 9930–9940.
- (21) Dürrenberger, M.; Ward, T. R. Recent Achievements in the Design and Engineering of Artificial Metalloenzymes. *Curr. Opin. Chem. Biol.* **2014**, *19*, 99–106.
- (22) Brodin, J. D.; Smith, S. J.; Carr, J. R.; Tezcan, F. A. Designed, Helical Protein Nanotubes with Variable Diameters from a Single Building Block. *J. Am. Chem. Soc.* **2015**, *137*, 10468–10471.
- (23) Brodin, J. D.; Ambroggio, X. I.; Tang, C.; Parent, K. N.; Baker, T. S.; Tezcan, F. A. Metal-Directed, Chemically Tunable Assembly of One-, Two- and Three-Dimensional Crystalline Protein Arrays. *Nat. Chem.* **2012**, *4*, 375–382.
- (24) Bailey, J. B.; Subramanian, R. H.; Churchfield, L. A.; Tezcan, F. A. Metal-Directed Design of Supramolecular Protein Assemblies. *Methods Enzymol.* **2016**, *580*, 223–250.
- (25) Sherlock, J. C.; Smart, G. A. Tin in Foods and the Diet. *Food Addit. Contam.* **1984**, *1*, 277–282.
- (26) Blunden, S.; Wallace, T. Tin in Canned Food: A Review and Understanding of Occurrence and Effect. *Food Chem. Toxicol.* **2003**, *41*, 1651–1662.
- (27) Drummond, G. S.; Galbraith, R. A.; Sardana, M. K.; Kappas, A. Reduction of the C2 and C4 Vinyl Groups of Sn-Protoporphyrin to Form Sn-Mesoporphyrin Markedly Enhances the Ability of the Metalloporphyrin to Inhibit *In Vivo* Heme Catabolism. *Arch. Biochem. Biophys.* **1987**, *255*, 64–74.
- (28) Ou, J. Z.; Ge, W.; Carey, B.; Daeneke, T.; Rotbart, A.; Shan, W.; Wang, Y.; Fu, Z.; Chrimes, A. F.; Wlodarski, W.; Russo, S. P.; Li, Y. X.; Kalantar-zadeh, K. Physisorption-Based Charge Transfer in Two-Dimensional SnS<sub>2</sub> for Selective and Reversible NO<sub>2</sub> Gas Sensing. *ACS Nano* **2015**, *9*, 10313–10323.
- (29) Zhong, H.; Yang, G.; Song, H.; Liao, Q.; Cui, H.; Shen, P.; Wang, C. X. Vertically Aligned Graphene-like SnS<sub>2</sub> Ultrathin Nanosheet Arrays: Excellent Energy Storage, Catalysis, Photoconduction, and Field-Emitting Performances. *J. Phys. Chem. C* **2012**, *116*, 9319–9326.
- (30) Qin, R.; Liu, Y.; Tao, F.; Li, C.; Cao, W.; Yang, P. Protein-Bound Freestanding 2D Metal Film for Stealth Information Transmission. *Adv. Mater.* **2019**, *31*, 1803377.
- (31) Gao, A.; Wu, Q.; Wang, D.; Ha, Y.; Chen, Z.; Yang, P. A Superhydrophobic Surface Templated by Protein Self-Assembly and Emerging Application Toward Protein Crystallization. *Adv. Mater.* **2016**, *28*, 579–587.
- (32) Yang, P. Direct Biomolecule Binding on Nonfouling Surfaces via Newly Discovered Supramolecular Self-Assembly of Lysozyme under Physiological Conditions. *Macromol. Biosci.* **2012**, *12*, 1053–1059.
- (33) Wu, Z.; Yang, P. Simple Multipurpose Surface Functionalization by Phase Transited Protein Adhesion. *Adv. Mater. Interfaces* **2015**, *2*, 1400401.
- (34) Breydo, L.; Uversky, V. N. Role of Metal Ions in Aggregation of Intrinsically Disordered Proteins in Neurodegenerative Diseases. *Metallomics* **2011**, *3*, 1163–1180.
- (35) Stirpe, A.; Rizzuti, B.; Pantusa, M.; Bartucci, R.; Sportelli, L.; Guzzi, R. Thermally Induced Denaturation and Aggregation of BLG-A: Effect of the Cu<sup>2+</sup> and Zn<sup>2+</sup> Metal Ions. *Eur. Biophys. J.* **2008**, *37*, 1351–1360.
- (36) Zou, R.; Wang, Q.; Wu, J.; Wu, J.; Schmuck, C.; Tian, H. Peptide Self-Assembly Triggered by Metal Ions. *Chem. Soc. Rev.* **2015**, *44*, 5200–5219.
- (37) Zhang, Y.; Zhu, P.; Huang, L.; Xie, J.; Zhang, S.; Cao, G.; Zhao, X. Few-Layered SnS<sub>2</sub> on Few-Layered Reduced Graphene Oxide as Na-Ion Battery Anode with Ultralong Cycle Life and Superior Rate Capability. *Adv. Funct. Mater.* **2015**, *25*, 481–489.
- (38) Salgado, E. N.; Radford, R. J.; Tezcan, F. A. Metal-Directed Protein Self-Assembly. *Acc. Chem. Res.* **2010**, *43*, 661–672.
- (39) Lmoumène, C. E. H.; Conte, D.; Jacquot, J. P.; Houé-Levin, C. Redox Properties of Protein Disulfide Bond in Oxidized Thioredoxin and Lysozyme: A Pulse Radiolysis Study. *Biochemistry* **2000**, *39*, 9295–9301.
- (40) David, C.; Foley, S.; Enescu, M. Protein S–S Bridge Reduction: A Raman and Computational Study of Lysozyme Interaction with TCEP. *Phys. Chem. Chem. Phys.* **2009**, *11*, 2532–2542.

- (41) Bonnet, D.; Stevens, J. M.; Sousa, R. A. D.; Sari, M. A.; Mansuy, D.; Artaud, I. New Inhibitors of Iron-Containing Nitrile Hydratases. *J. Biochem.* **2001**, *130*, 227–233.
- (42) O'Halloran, T. V.; Culotta, V. C. Metallochaperones, an Intracellular Shuttle Service for Metal Ions. *J. Biol. Chem.* **2000**, *275*, 25057–25060.
- (43) Chang, K.; Wang, Z.; Huang, G.; Li, H.; Chen, W.; Lee, J. Y. Few-Layer SnS<sub>2</sub>/Graphene Hybrid with Exceptional Electrochemical Performance as Lithium-Ion Battery Anode. *J. Power Sources* **2012**, *201*, 259–266.
- (44) Chang, K.; Chen, W. X.; Li, H.; Li, H. Microwave-Assisted Synthesis of SnS<sub>2</sub>/SnO<sub>2</sub> Composites by L-cysteine and Their Electrochemical Performances When Used as Anode Materials of Li-Ion Batteries. *Electrochim. Acta* **2011**, *56*, 2856–2861.
- (45) Zai, J.; Qian, X.; Wang, K.; Yu, C.; Tao, L.; Xiao, Y.; Chen, J. 3D-Hierarchical SnS<sub>2</sub> Micro/Nano-Structures: Controlled Synthesis, Formation Mechanism and Lithium Ion Storage Performances. *CrystEngComm* **2012**, *14*, 1364–1375.
- (46) Zhao, L.; Di, Y.; Yan, C.; Liu, F.; Cheng, Z.; Jiang, L.; Hao, X.; Lai, Y.; Li, J. *In Situ* Growth of SnS Absorbing Layer by Reactive Sputtering for Thin Film Solar Cells. *RSC Adv.* **2016**, *6*, 4108–4115.
- (47) Miflin, B. J. Amino Acids and Derivatives, 1st ed.; *The Biochemistry of Plants*; Academic Press, 1980; pp 255.
- (48) Wang, C.; Tang, K.; Yang, Q.; Qian, Y. Raman Scattering, Far Infrared Spectrum and Photoluminescence of SnS<sub>2</sub> Nanocrystallites. *Chem. Phys. Lett.* **2002**, *357*, 371–375.
- (49) Ma, D.; Zhou, H.; Zhang, J.; Qian, Y. Controlled Synthesis and Possible Formation Mechanism of Leaf-Shaped SnS<sub>2</sub> Nanocrystals. *Mater. Chem. Phys.* **2008**, *111*, 391–395.
- (50) Gu, J.; Miao, S.; Yan, Z.; Yang, P. Multiplex Binding of Amyloid-Like Protein Nanofilm to Different Material Surfaces. *Colloid Interface Sci. Commun.* **2018**, *22*, 42–48.
- (51) Umar, A.; Akhtar, M. S.; Dar, G. N.; Abaker, M.; Al-Hajry, A.; Baskoutas, S. Visible-Light-Driven Photocatalytic and Chemical Sensing Properties of SnS<sub>2</sub> Nanoflakes. *Talanta* **2013**, *114*, 183–190.
- (52) Seo, J.; Hoffmann, W.; Warnke, S.; Huang, X.; Gewinner, S.; Schöllkopf, W.; Pagel, K. An Infrared Spectroscopy Approach to Follow  $\beta$ -sheet Formation in Peptide Amyloid Assemblies. *Nat. Chem.* **2017**, *9*, 39–44.
- (53) Nandan, B.; Venugopal, B.; Amirthapandian, S.; Panigrahi, B.; Thangadurai, P. Effect of Pd Ion Doping in the Band Gap of SnO<sub>2</sub> Nanoparticles: Structural and Optical Studies. *J. Nanopart. Res.* **2013**, *15*, 1999.
- (54) Guo, Y.; Tan, R.; Li, X.; Zhao, J.; Luo, Z.; Gao, C.; Song, W. Shape-Controlled Growth and Single-Crystal XRD Study of Submillimeter-Sized Single Crystals of SnO. *CrystEngComm* **2011**, *13*, 5677–5680.
- (55) Li, Q.; Wang, Z.; Zhang, M.; Hou, P.; Kang, P. Nitrogen Doped Tin Oxide Nanostructured Catalysts for Selective Electrochemical Reduction of Carbon Dioxide to Formate. *J. Energy Chem.* **2017**, *26*, 825–829.
- (56) Xie, J.; Qin, M.; Cao, Y.; Wang, W. Mechanistic Insight of Photo-Induced Aggregation of Chicken Egg White Lysozyme: The Interplay Between Hydrophobic Interactions and Formation of Intermolecular Disulfide Bonds. Proteins: Structure, Function, and Bioinformatics. *Proteins: Struct., Funct., Genet.* **2011**, *79*, 2505–2516.
- (57) Chimon, S.; Shaibat, M. A.; Jones, C. R.; Calero, D. C.; Aizezi, B.; Ishii, Y. Evidence of Fibril-Like  $\beta$ -sheet Structures in a Neurotoxic Amyloid Intermediate of Alzheimer's  $\beta$ -Amyloid. *Nat. Struct. Mol. Biol.* **2007**, *14*, 1157–1164.
- (58) Lee, J.; Choe, I. R.; Kim, N. K.; Kim, W. J.; Jang, H. S.; Lee, Y. S.; Nam, K. T. Water-Floating Giant Nanosheets from Helical Peptide Pentamers. *ACS Nano* **2016**, *10*, 8263–8270.
- (59) Abe, H.; Matsue, T.; Yabu, H. Reversible Shape Transformation of Ultrathin Polydopamine-Stabilized Droplet. *Langmuir* **2017**, *33*, 6404–6409.
- (60) Pieranski, P. Two-Dimensional Interfacial Colloidal Crystals. *Phys. Rev. Lett.* **1980**, *45*, 569–572.
- (61) Valle, R. P.; Wu, T.; Zuo, Y. Y. Biophysical Influence of Airborne Carbon Nanomaterials on Natural Pulmonary Surfactant. *ACS Nano* **2015**, *9*, 5413–5421.
- (62) Li, C.; Xu, L.; Zuo, Y. Y.; Yang, P. Tuning Protein Assembly Pathways through Superfast Amyloid-Like Aggregation. *Biomater. Sci.* **2018**, *6*, 836–841.
- (63) Song, Y.; Shimanovich, U.; Michaels, T. C.; Ma, Q.; Li, J.; Knowles, T. P.; Shum, H. C. Fabrication of Fibrillosomes from Droplets Stabilized by Protein Nanofibrils at All-Aqueous Interfaces. *Nat. Commun.* **2016**, *7*, 12934.
- (64) Szilvay, G. R.; Paananen, A.; Laurikainen, K.; Vuorimaa, E.; Lemmetyinen, H.; Peltonen, J.; Linder, M. B. Self-Assembled Hydrophobin Protein Films at the Air-Water Interface: Structural Analysis and Molecular Engineering. *Biochemistry* **2007**, *46*, 2345–2354.
- (65) Jang, H.-S.; Lee, J.-H.; Park, Y.-S.; Kim, Y.-O.; Park, J.; Yang, T.-Y.; Jin, K.; Lee, J.; Park, S.; You, J. M.; Jeong, K.-W.; Shin, A.; Oh, I.-S.; Kwon, M.-K.; Kim, Y.-I.; Cho, H. H.; Han, H. N.; Kim, Y.; Chang, Y. H.; Paik, S. R.; et al. Tyrosine-Mediated Two-Dimensional Peptide Assembly and Its Role as a Bio-Inspired Catalytic Scaffold. *Nat. Commun.* **2014**, *5*, 3665.
- (66) Zhao, J.; Qu, Y.; Chen, H.; Xu, R.; Yu, Q.; Yang, P. Self-Assembled Proteinaceous Wound Dressings Attenuate Secondary Trauma and Improve Wound Healing *In Vivo*. *J. Mater. Chem. B* **2018**, *6*, 4645–4655.
- (67) Fakhri, A.; Behrouz, S. Assessment of SnS<sub>2</sub> Nanoparticles Properties for Photocatalytic and Antibacterial Applications. *Sol. Energy* **2015**, *117*, 187–191.
- (68) Khimani, A. J.; Chaki, S. H.; Chauhan, S. M.; Mangrola, A. V.; Meena, R. R.; Deshpande, M. P. Synthesis, Characterization, Antimicrobial and Antioxidant Study of the Facile Sonochemically Synthesized SnS<sub>2</sub> Nanoparticles. *Nano-Struct. Nano-Objects.* **2019**, *18*, 100286.
- (69) Meena Kumari, M.; Philip, D. Synthesis of Biogenic SnO<sub>2</sub> Nanoparticles and Evaluation of Thermal, Rheological, Antibacterial and Antioxidant Activities. *Powder Technol.* **2015**, *270*, 312–319.
- (70) Ibrahim, H. R.; Higashiguchi, S.; Koketsu, M.; Juneja, L. R.; Kim, M.; Yamamoto, T.; Sugimoto, Y.; Aoki, T. Partially Unfolded Lysozyme at Neutral pH Agglutinates and Kills Gram-Negative and Gram-Positive Bacteria through Membrane Damage Mechanism. *J. Agric. Food Chem.* **1996**, *44*, 3799–3806.
- (71) Muszanska, A. K.; Busscher, H. J.; Herrmann, A.; van der Mei, H. C.; Norde, W. Pluronic–Lysozyme Conjugates as Anti-Adhesive and Antibacterial Bifunctional Polymers for Surface Coating. *Biomaterials* **2011**, *32*, 6333–6341.
- (72) Nepal, D.; Balasubramanian, S.; Simonian, A. L.; Davis, V. A. Strong Antimicrobial Coatings: Single-Walled Carbon Nanotubes Armored with Biopolymers. *Nano Lett.* **2008**, *8*, 1896–1901.
- (73) Cegielska-Radziejewska, R.; Lesnierowski, G.; Kijowski, J. Antibacterial Activity of Hen Egg White Lysozyme Modified by Thermochemical Technique. *Eur. Food Res. Technol.* **2009**, *228*, 841–845.
- (74) Lesnierowski, G.; Kijowski, J.; Cegielska-Radziejewska, R. Ultrafiltration-Modified Chicken Egg White Lysozyme and Its Antibacterial Action. *Int. J. Food Sci. Technol.* **2009**, *44*, 305–311.
- (75) Gu, J.; Su, Y.; Liu, P.; Li, P.; Yang, P. An Environmentally Benign Antimicrobial Coating Based on a Protein Supramolecular Assembly. *ACS Appl. Mater. Interfaces* **2017**, *9*, 198–210.
- (76) Ha, Y.; Yang, J.; Tao, F.; Wu, Q.; Song, Y.; Wang, H.; Yang, P. Phase-Transited Lysozyme as a Universal Route to Bioactive Hydroxyapatite Crystalline Film. *Adv. Funct. Mater.* **2018**, *28*, 1704476.
- (77) Gruenwedel, D. W.; Hao, H. C. Model Studies Regarding the Internal Corrosion of Tin-Plated Food Cans. III. Binding of Tin (II) Ions and Iron (II) Ions by Sulfur-Containing Amino Acids. *J. Agric. Food Chem.* **1973**, *21*, 246–251.
- (78) Sun, Y.; Cheng, H.; Gao, S.; Sun, Z.; Liu, Q.; Liu, Q.; Xie, Y. Freestanding Tin Disulfide Single-Layers Realizing Efficient Visible-Light Water Splitting. *Angew. Chem. Int. Ed.* **2012**, *124*, 8727–8731.

- (79) Müller, M.; Zentel, R.; Maka, T.; Romanov, S. G.; Sotomayor Torres, C. M. Photonic Crystal Films with High Refractive Index Contrast. *Adv. Mater.* **2000**, *12*, 1499–1503.
- (80) Panda, S. K.; Antonakos, A.; Liarakis, E.; Bhattacharya, S.; Chaudhuri, S. Optical Properties of Nanocrystalline SnS<sub>2</sub> Thin Films. *Mater. Res. Bull.* **2007**, *42*, 576–583.
- (81) Huang, Y.; Sutter, E.; Sadowski, J. T.; Cotlet, M.; Monti, O. L. A.; Racke, D. A.; Neupane, M. R.; Wickramaratne, D.; Lake, R. K.; Parkinson, B. A.; Sutter, P. Tin Disulfide-An Emerging Layered Metal Dichalcogenide Semiconductor: Materials Properties and Device Characteristics. *ACS Nano* **2014**, *8*, 10743–10755.
- (82) Liu, G.; Li, Z.; Hasan, T.; Chen, X.; Zheng, W.; Feng, W.; Hu, P. Vertically Aligned Two-Dimensional SnS<sub>2</sub> Nanosheets with a Strong Photon Capturing Capability for Efficient Photoelectrochemical Water Splitting. *J. Mater. Chem. A* **2017**, *5*, 1989–1995.
- (83) Saidman, S. B.; Bessone, J. B. Electrochemical Preparation and Characterisation of Polypyrrole on Aluminium in Aqueous Solution. *J. Electroanal. Chem.* **2002**, *521*, 87–94.
- (84) Gutiérrez Pineda, E.; Alcaide, F.; Rodríguez Presa, M. J.; Bolzán, A. E.; Gervasi, C. A. Electrochemical Preparation and Characterization of Polypyrrole/Stainless Steel Electrodes Decorated with Gold Nanoparticles. *ACS Appl. Mater. Interfaces* **2015**, *7*, 2677–2687.
- (85) Ensafi, A. A.; Ahmadi, N.; Rezaei, B. Electrochemical Preparation and Characterization of a Polypyrrole/Nickel-Cobalt Hexacyanoferrate Nanocomposite for Supercapacitor Applications. *RSC Adv.* **2015**, *5*, 91448–91456.
- (86) Firbank, S. J.; Rogers, M. S.; Wilmot, C. M.; Dooley, D. M.; Halcrow, M. A.; Knowles, P. F.; McPherson, M. J.; Phillips, S. E. V. Crystal Structure of the Precursor of Galactose Oxidase: An Unusual Self-Processing Enzyme. *Proc. Natl. Acad. Sci. U. S. A.* **2001**, *98*, 12932–12937.
- (87) Yang, Y.; Wang, C.; Yue, B.; Gambhir, S.; Too, C. O.; Wallace, G. G. Electrochemically Synthesized Polypyrrole/Graphene Composite Film for Lithium Batteries. *Adv. Energy Mater.* **2012**, *2*, 266–272.
- (88) Mondal, P.; Sinha, A.; Salam, N.; Roy, A. S.; Jana, N. R.; Islam, S. M. Enhanced Catalytic Performance by Copper Nanoparticle–Graphene Based Composite. *RSC Adv.* **2013**, *3*, 5615–5623.
- (89) Sontz, P. A.; Song, W. J.; Tezcan, F. A. Interfacial Metal Coordination in Engineered Protein and Peptide Assemblies. *Curr. Opin. Chem. Biol.* **2014**, *19*, 42–49.
- (90) Savelieff, M. G.; DeToma, A. S.; Derrick, J. S.; Lim, M. H. The Ongoing Search for Small Molecules to Study Metal-Associated Amyloid- $\beta$  Species in Alzheimer's Disease. *Acc. Chem. Res.* **2014**, *47*, 2475–2482.
- (91) Raman, B.; Ban, T.; Yamaguchi, K. I.; Sakai, M.; Kawai, T.; Naiki, H.; Goto, Y. Metal Ion-Dependent Effects of Clonidine on the Fibril Growth of an Amyloid  $\beta$  Peptide. *J. Biol. Chem.* **2005**, *280*, 16157–16162.
- (92) Yoshiike, Y.; Tanemura, K.; Murayama, O.; Akagi, T.; Murayama, M.; Sato, S.; Sun, X.; Tanaka, N.; Takashima, A. New Insights on How Metals Disrupt Amyloid  $\beta$ -Aggregation and Their Effects on Amyloid- $\beta$  Cytotoxicity. *J. Biol. Chem.* **2001**, *276*, 32293–32299.
- (93) Liu, R.; Zhao, J.; Han, Q.; Hu, X.; Wang, D.; Zhang, X.; Yang, P. One-Step Assembly of a Biomimetic Biopolymer Coating for Particle Surface Engineering. *Adv. Mater.* **2018**, *30*, 1802851.
- (94) Zhu, S.; Sun, H.; Geng, H.; Liu, D.; Zhang, X.; Cai, Q.; Yang, X. Dual Functional Polylactide–Hydroxyapatite Nanocomposites for Bone Regeneration with Nano-Silver Being Loaded *via* reductive polydopamine. *RSC Adv.* **2016**, *6*, 91349–91360.
- (95) Qi, X.; Zhang, J.; Yuan, H.; Xu, Z.; Li, Q.; Niu, X.; Li, X. Exosomes Secreted by Human-Induced Pluripotent Stem Cell-Derived Mesenchymal Stem Cells Repair Critical-Sized Bone Defects through Enhanced Angiogenesis and Osteogenesis in Osteoporotic Rats. *Int. J. Biol. Sci.* **2016**, *12*, 836.
- (96) Hoang, S.; Guo, S.; Hahn, N. T.; Bard, A. J.; Mullins, C. B. Visible Light Driven Photoelectrochemical Water Oxidation on Nitrogen-Modified TiO<sub>2</sub> Nanowires. *Nano Lett.* **2012**, *12*, 26–32.
- (97) LeVine, H., III Quantification of  $\beta$ -Sheet Amyloid Fibril Structures with Thioflavin T. *Methods Enzymol.* **1999**, *309*, 274–284.
- (98) Málnási-Csizmadia, A.; Hegyi, G.; Tölgyesi, F.; Szent-Györgyi, A. G.; Nyitrai, L. Fluorescence Measurements Detect Changes in Scallop Myosin Regulatory Domain. *Eur. J. Biochem.* **1999**, *261*, 452–458.